



Effect of layered joints on rockburst in deep tunnels

Mingming He^{1,2} · Jinrui Zhao^{1,2} · Bianyuan Deng³ · Zhiqiang Zhang^{1,2}

Received: 9 September 2021 / Accepted: 9 March 2022
© The Author(s) 2022

Abstract

The existence of joints in the surrounding rock mass has a considerable effect on tunnel rockbursts. Herein, we studied the effect of layered joints with different inclination angles and spacings on rockburst in deep tunnels and investigated the failure area, deformation process of the surrounding rock mass, stress change inside the surrounding rock mass, velocity of the failed rock, and the kinetic energy of the failure. The failure type of the surrounding rock mass can thus be determined. The results showed that the intensity of rockburst increases as rock quality designation (RQD) decreases, while the deformation rate of the surrounding rock mass first increases and then decreases. The deformation rate exhibits a turning point between RQD = 50 and 70, below which the deformation rate of the surrounding rock mass gradually decreases, ultimately ceasing to be a rockburst. Rockburst always occurs perpendicular to the direction of the joint. When $\sigma_x = \sigma_y$, as the joint inclination angle changes from 45° to 90°, the intensity of a rockburst first decreases (from 45° to 60°), and then increases (from 60° to 90°). When combined with the evolution law of stress and strain energy, the rockburst process can be divided into four stages.

Keywords Rockburst · Jointed rock mass · Numerical simulation · Deep tunnel

1 Introduction

Rockbursts usually occur in hard rock areas with high in situ stress (Chen et al. 2014; Gong et al. 2018a, 2018b, 2019, 2020; Feng et al. 2015, 2021; Christopher 2016; He et al. 2020). The number of rockburst incidences increases with the excavation depth (Zhang et al. 2021; Gao et al. 2021; Dou et al. 2021; Wang et al. 2020; Chen 2020). A rockburst is accompanied by a high-speed ejection of the rock block, which can have disastrous consequences (Su et al. 2016, 2017). Rockbursts pose a serious threat to worker safety and investment (Dowding and Andersson 1986, Cai 2013; Chen et al. 1997; Whyatt et al. 2002; Zhang et al. 2013; Zhu et al.

2009; He et al. 2021a, b), and numerous efforts have been made to understand their mechanisms.

In recent years, with the gradual increase in mining depths and excavation activities, the number of rockburst incidences around the world has increased (Leger 1991; Gu et al. 2002; Chen et al. 2021; Itasca Consulting Group Inc. 2016; Jian et al. 2012). To address this problem, numerous scholars (Tan et al. 1990; Zhou et al. 2014; Charlie 2021; Zhu and Song 2003) have examined the theories of energy, strength, stiffness, instability, damage, fault failure, and coupled failure to explain the causes of rockbursts. These studies show that a rockburst is a sudden dynamic failure phenomenon, and the current solution is to predict their location and intensity. Several scholars (Zhang and Fu 2008; Xu and Wang 2001) have proposed a number of rockburst models to predict these occurrences. However, the actual working conditions are very complex. There are numerous factors that affect rockbursts (Lee et al. 2004; Mansurov 2001; Wang and Park 2001; Kaiser and Cai 2012), the four main factors being seismic events, geology, geotechnical properties, and mining activity. Studies have been conducted on the impact of these factors on rockbursts (Kaiser et al. 1996; Reddy and Spottiswoode 2001; Salamon 1983; Zhang et al. 2013; Zhu et al. 2010). Among them, the joint has a crucial influence on the rockburst, which is more likely to occur when

✉ Mingming He
hemingming@xaut.edu.cn

¹ State Key Laboratory of Eco-Hydraulics in Northwest Arid Region, Xi'an University of Technology, Xi'an 710048, China

² Shaanxi Key Laboratory of Loess Mechanics and Engineering, Xi'an University of Technology, Xi'an 710048, China

³ YCIH Foundation Engineering Co., Ltd., Kunming 657200, China

there is a joint near the surrounding rock of a tunnel (Hedley 1992; Paige et al. 2013; Zhang et al. 2013; Zhou et al. 2014; Zhou et al. 2015; Feng et al. 2019; Amin and Cai 2018). According to on-site monitoring and analysis of moderate and strong rockbursts, most are affected by structural planes (Feng et al. 2019). Numerous rockburst cases affected by weak planes can be categorized into slip, shear fracture, and tensioning slab crack types (Zhou et al. 2015; Jiang et al. 2021a, b). However, it is difficult to ascertain the stress and energy changes in the rockburst process by field monitoring. Numerical simulations have been used to study unstable rock failures near underground openings (Jiang et al. 2010, 2015; Kias and Ozbay 2013; Zhang et al. 2014). The above studies explain rockbursts near tunnels from a number of perspectives. It is still unclear what effects joints have on rockbursts.

In this study, we employ the particle flow code software (PFC2D) to investigate the effect of joints on rockbursts in deep tunnels (Cheng 2012; Wu 2019). We obtain the deformation process of the surrounding rock and the evolution law of stress and strain energy from excavation to rockburst. The influences of the inclined angle θ and spacing d of the joints and the initial ground stress on rockbursts are studied. Finally, we summarize the variation law of stress with time in the surrounding rock corresponding to rockbursts of different intensities. The research results aid in establishing a more intuitive understanding of the rockburst process and in establish a prediction model for rockbursts in jointed rock masses.

2 Model setup and tunnel excavation simulation method

A rockburst is a typical dynamic failure phenomenon. We construct the discrete element method based on dynamic theory, which is suitable for the simulation of complex dynamic phenomena. PFC2D uses the discrete element method to simulate the motion of circular particles and the interactions among them, which effectively simulates the failure process of a rockburst.

2.1 Model setup

2.1.1 Contact model principle of PFC software

PFC2D simulates the contact between particles and distinguishes different materials by choosing the type of contact and assigning different parameters to it. Numerous studies have shown that the linear parallel bond model is suitable for simulating hard rock (Qiu et al. 2020a). The principle of the linear parallel bond model (Fig. 1a) can be regarded as adding cement material at the contact position, which transfers both force and momentum. We employed this model to

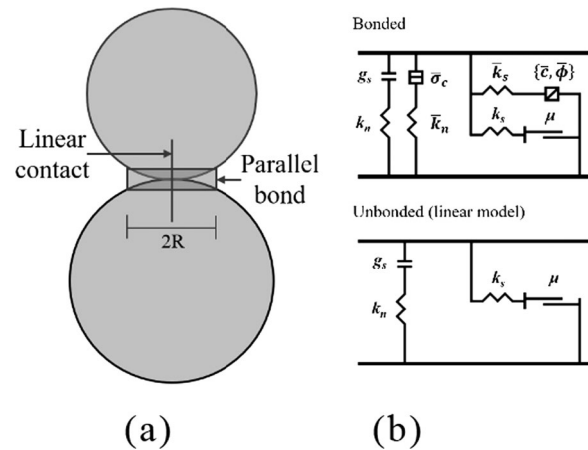


Fig. 1 Linear parallel bond model (Itasca 2016)

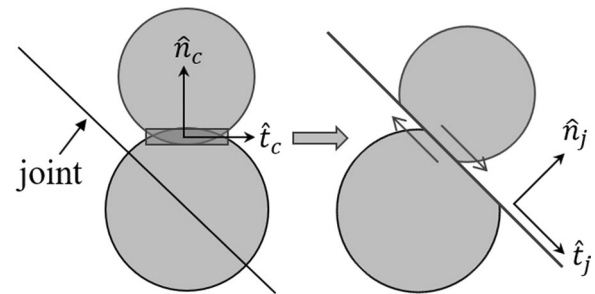


Fig. 2 Smooth joint model (Itasca 2016)

simulate the rock medium in this experiment. Its mechanical components are shown in Fig. 1b. This contact model is composed of linear contacts and parallel bonds. The parallel bond breaks when the stress reaches the strength limit of the bond, at which time the model is equivalent to the linear model. Smooth joint models are used to simulate joints in a rock mass. When a smooth joint model is added to the model, the contacts on both sides of all particles passed by the joint are transformed into a smooth joint model, and its parameters are reassigned. After the contact model is changed, the particles can slide along the direction of the joint (Fig. 2).

2.1.2 Model setting and parameter calibration

The rockburst simulation caused by tunnel excavation proceeds through two stages. In the first stage, the initial in situ stress is simulated by applying gravity and controlling the movement of the upper, left, and right walls to squeeze the particles. When the internal stress of the model reaches the preset value, and the unbalanced force between particles is less than or equal to 10^{-5} , the loading is stopped. In this process, a stress measurement circle is

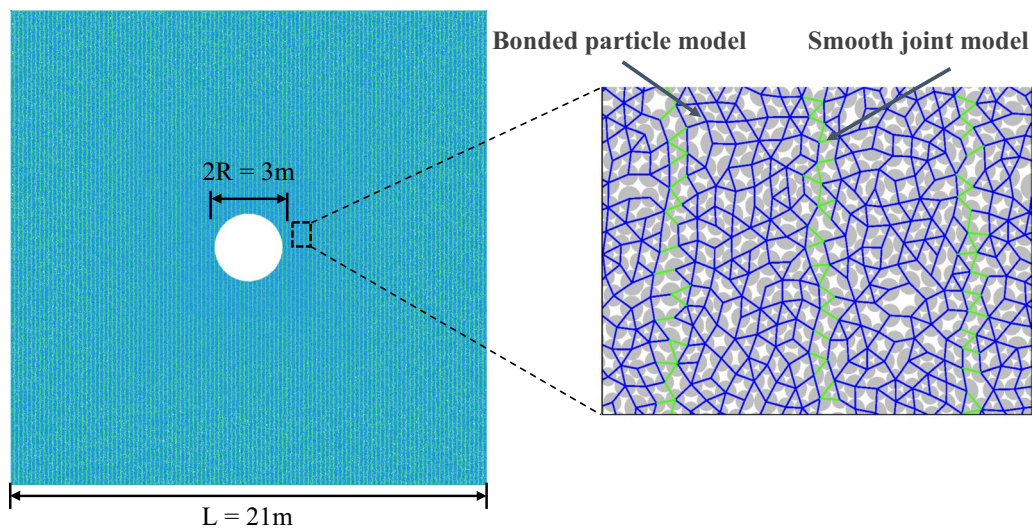


Fig. 3 Model diagram. Note: the green line represent the joints

Table 1 Particle size table of different regions of the model

Zone (m)	R_{min} (mm)	R_{max} (mm)	Number of balls
6×6	10	15	61,571
10×10	15	20	56,390
14×14	20	25	51,126
21×21	25	30	87,845

placed at the center of the model to determine whether the stress in the x - and y -directions reaches the requirements after the model is loaded. It is confirmed that the initial in situ stress reaches the preset value. In the second stage, all particles in a 3 m diameter circular area at the center of the model are removed to simulate tunnel excavation. At this stage, the stress on the wall remains stable (Qiu et al. 2020b; Wu 2019).

Table 2 Microscopic parameter values of parallel bonding model

Type	Item	Value
Ball parameter	Ball density (kg/m^3)	2500
	Modulus E (GPa)	24.15
	Stiffness ratio k_n/k_s	3
Parallel bond parameter	Friction coefficient μ	0
	Modulus E (GPa)	24.15
	Stiffness ratio k_n/k_s	3
	Tensile strength (MPa)	155
	Cohesion (MPa)	155

The size of the model was 21 m×21 m (Fig. 3); the diameter of the simulated tunnel was 3 m, and a total of 256,746 particles were included in the model. Due to the small joint spacing, the particle size must be sufficiently small to obtain

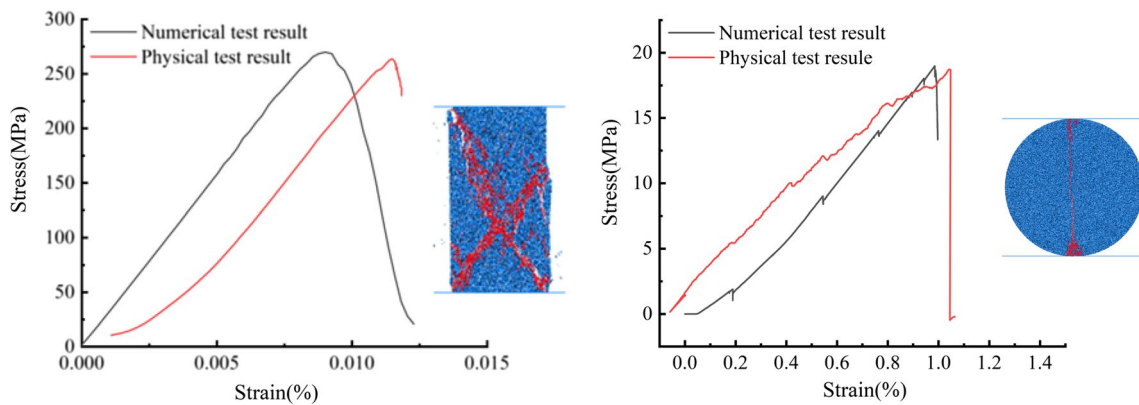
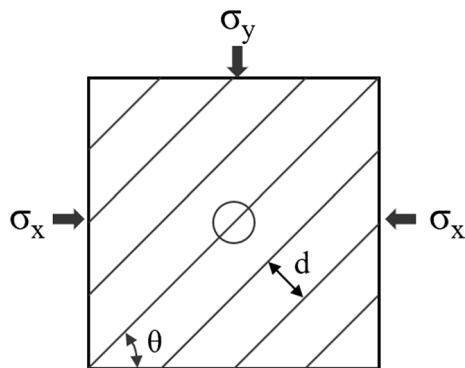


Fig. 4 Uniaxial compression test and split test results

Table 3 Values of microscopic parameters in numerical simulation

Test	Uniaxial compressive strength (MPa)	Tensile strength (MPa)	Modulus of elasticity (GPa)
Laboratory test	261.25	18.74	31.52
Numerical simulation test	270.11	18.99	31.52

**Fig. 5** Schematic diagram of the scheme

a good simulation effect. Therefore, the method of gradually increasing the particle size is adopted to allocate different particle sizes to different areas (Table 1), which can reduce the calculation burden and provide more accurate simulation results near the tunnel (John et al. 2009).

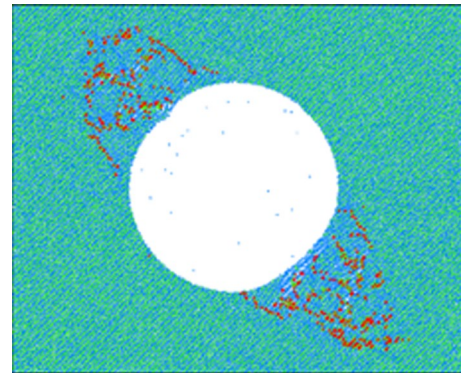
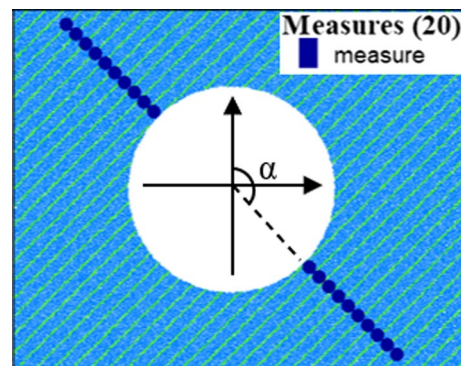
The granite block was processed into $\Phi 50 \text{ mm} \times 100 \text{ mm}$ and $\Phi 50 \text{ mm} \times 25 \text{ mm}$ (ISRM) standard specimens, and the uniaxial compression test and split test were performed to obtain the stress–strain curve. Rock samples of the same size were established in the software for the uniaxial compression test and split test. The different parameters of the linear parallel bond model were adjusted continuously by the "trial and error method" (Potyondy and Cundall 2004) to make its stress–strain curve and failure mode similar to the actual rock (Fig. 4). The microscopic parameters of the parallel bond model and the mechanical parameters are summarized in Tables 2 and 3. Table 4 summarizes the microscopic parameters of the smooth joint model (Huan 2021).

2.2 Experimental scheme

This numerical simulation mainly studies the influences of the initial in situ stress, joint inclination θ , and joint spacing d on tunnel rockbursts. Four different joint inclined angles θ (45° , 60° , 75° , and 90°) were added to the model, and each joint inclined angle had five different

Table 4 Values of microscopic parameters of smooth joint model

Normal stiffness (sj_kn) (GPa/m)	Shear stiffness (sj_ks) (GPa/m)	Friction coefficient (sj_fric)
200	50	0.8

**Fig. 6** Schematic diagram of failure location**Fig. 7** Arrangement of measuring points

joint spacings d (6.0, 7.3, 9.2, 12.2, and 19.0 cm). The joint spacing was obtained by RQDs of 50, 60, 70, 80, and 90 through the conversion formula of the fracture frequency (Eq. (1)), and 20 rock models with different joints were established. Deep tunnels are usually subjected to upper earth pressure and horizontal tectonic stress; hence, biaxial loading is used for the model (Fig. 5). Different initial in situ stresses were simulated by changing the lateral pressure σ_x and the vertical stress σ_y . A total of five initial in situ stress conditions, $\sigma_x = \sigma_y$ ($\sigma_x = \sigma_y = 30, 50$, and 70 MPa) and $\sigma_x \neq \sigma_y$ ($\sigma_y = 50 \text{ MPa}$, $\sigma_x = 25$ and 75 MPa), were simulated. However, due to the long calculation time required, it is difficult to carry out a large number of calculations for each scheme. Therefore, most models were calculated to 0.085 s after excavation, and only individual cases were calculated to 0.6 s.

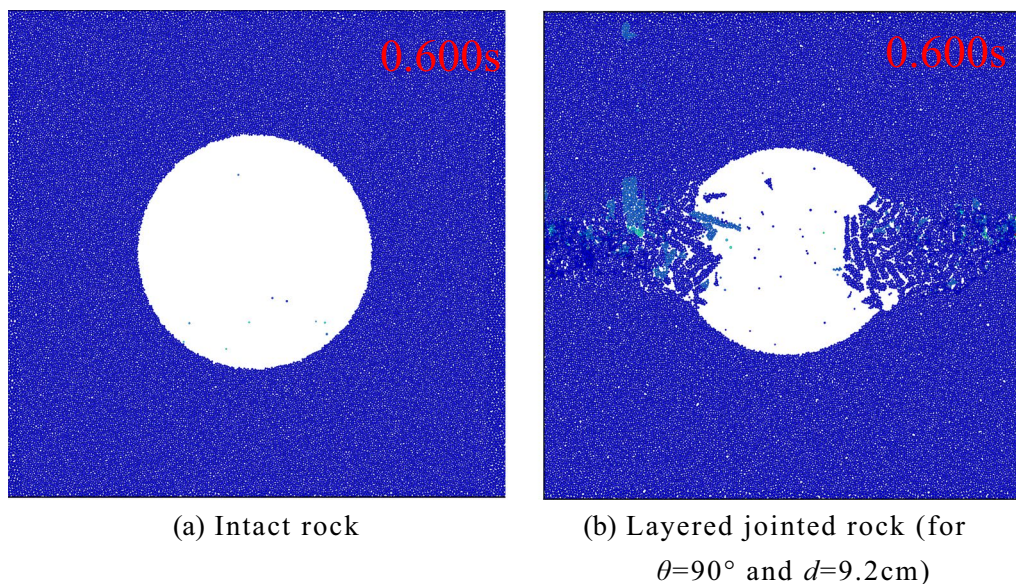


Fig. 8 Comparison diagram of failure results (for $\sigma_x=\sigma_y=70$ MPa)

Priest and Hudson (1976) derived the relationship between fracture frequency λ and RQD, as shown in Eq. (1):

$$\text{RQD} = 100e^{-\lambda t}(\lambda t + 1) \tag{1}$$

where t is the length threshold ($t=0.1$ m).

2.3 Monitoring program

In this numerical simulation, the change in the surrounding rock during the failure process, the change in stress and velocity at the point of failure, and the overall kinetic energy of the model were recorded to identify whether a rockburst occurred and determine its intensity. First, the position and velocity of particles in the model were saved every 0.005 s (the physical time calculated in the software) to observe the processes of deformation and failure of the surrounding rock. Second, after several trial calculations, it was found that the tunnel was always damaged perpendicular to the joint after excavation (Fig. 6). Therefore, twenty measuring circles and velocity measurement points (Fig. 7) were arranged along the perpendicular direction of the joint. The radius of the measuring circles was 10 cm to enable recording the change process of the stress (σ_x , σ_y , and τ_{xy}) in the region from the moment of excavation start to the damage. The velocity measurement point was selected at 1 cm in the surrounding rock perpendicular to the direction of the joint. The kinetic energy change of the whole model was monitored after excavation, as the failure range could not be predicted. Thus, the maximum kinetic energy KE_{\max} of the layered joint model was obtained. By using KE_{\max} to subtract the maximum kinetic energy KE''_{\max} of the intact rock model

(no failure) to reduce the influence of particle movement in the nonfailure area on the kinetic energy, the kinetic energy KE' in the case of rockburst failure could be estimated.

The radial and tangential stresses (σ_r and σ_θ) at the measuring circles are calculated by Eq. (2) (Qiu et al. 2020b).

$$\begin{cases} \sigma_r = \sigma_x \sin^2 \alpha + \sigma_y \cos^2 \alpha + 2\tau_{xy} \sin \alpha \cos \alpha \\ \sigma_\theta = \sigma_x \cos^2 \alpha + \sigma_y \sin^2 \alpha - 2\tau_{xy} \sin \alpha \cos \alpha \end{cases} \tag{2}$$

where α is the angle between the line connecting the circle, center of the tunnel, and the Y axis (Fig. 7).

The kinetic energy of rockburst is estimated by Eq. (3).

$$KE' = KE_{\max} + KE''_{\max} \tag{3}$$

where KE_{\max} is the maximum kinetic energy of the layered joint model after excavation, and KE''_{\max} is the maximum kinetic energy of the intact rock model.

3 Results

3.1 Influence of joints on tunnel rockburst

There is no failure of the surrounding rock in the rock model, and only a few particles are ejected (Fig. 8a). We note $V_{\max}=4.0$ m/s and $KE_{\max}=103$ kJ from the rock modeling results. In the layered jointed model, the surrounding rock on both sides of the tunnel is broken into blocks and ejected (Fig. 8b). For $V_{\max}=12.1$ m/s, $KE_{\max}=138$ kJ and $KE'=35$ kJ, the results indicate that strong rockburst occurred. Evidently, the joints in the surrounding rock can directly affect the occurrence of rockburst.

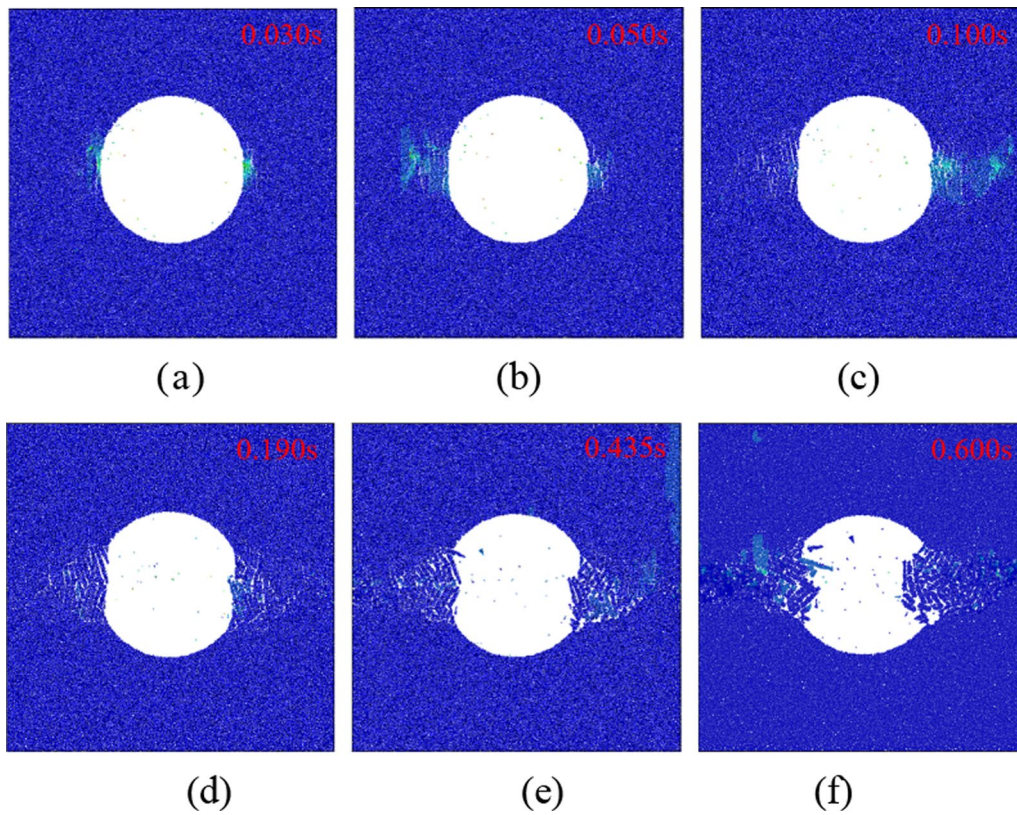


Fig. 9 Rockburst process

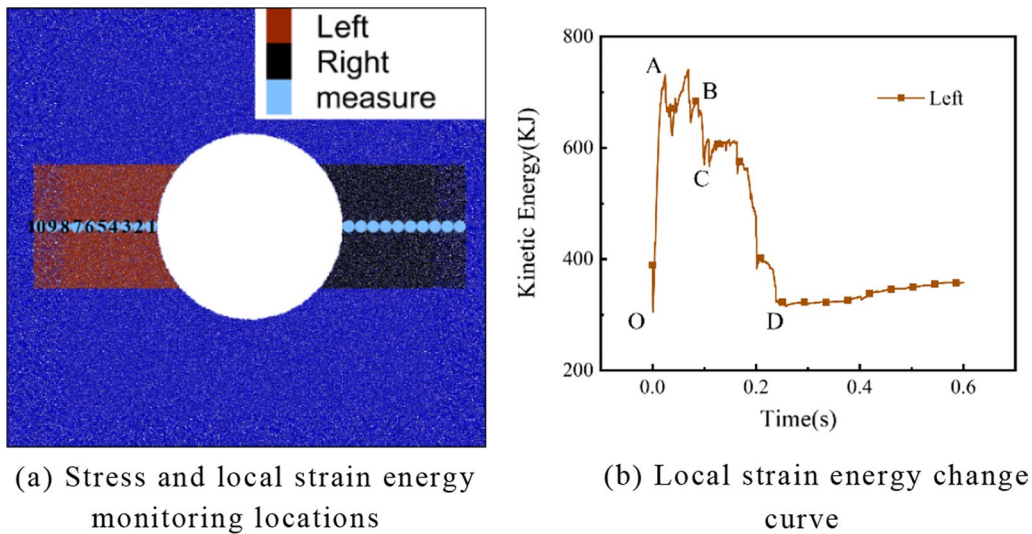


Fig. 10 Strain energy monitor

3.2 Rockburst process of layered jointed rock

Tan (1989) proposed three stages of tunnel rockburst: "splitting into slabs, fragmentation into blocks, and ejection." The failure mode is roughly the same as that of a tunnel with

joints in the surrounding rock, but the failure process is slightly different. When tunnel rockburst occurs, the surface rock mass is always destroyed first, after which the internal rock mass is split into slabs, broken into blocks, and ejected (Fig. 9).

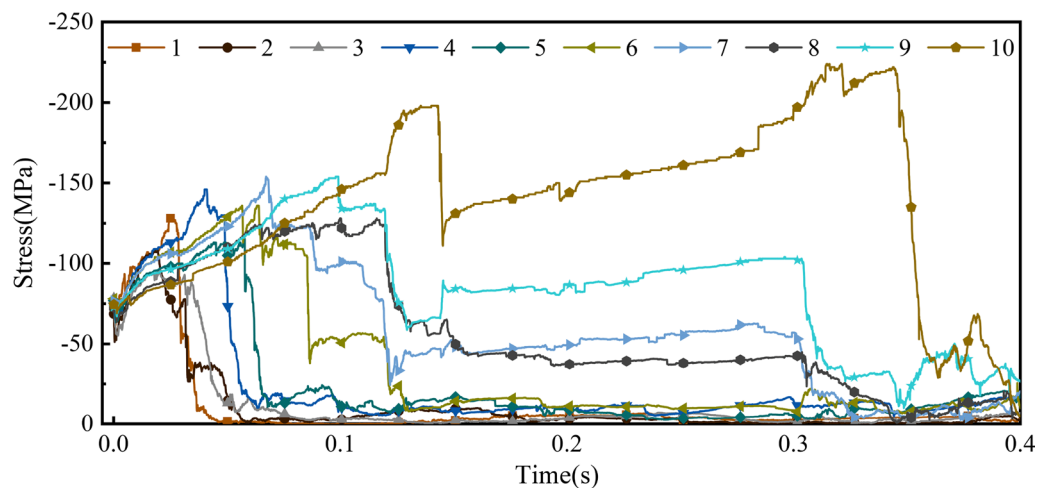


Fig. 11 Stress change diagram of the left wall

The range of rockburst damage can be obtained after completing the first calculation. The strain energy within the damage range can be monitored. The monitoring position is shown in Fig. 10a. According to the failure characteristics at different times in combination with the changes in stress (Fig. 10) and strain energy (Fig. 11), a rockburst in the layered jointed surrounding rock can be divided into the following four stages: slab buckling of the tunnel sidewall, internal rock mass splitting into slabs, internal slab fracture, and rock mass breakup and ejection.

Slab buckling of the tunnel sidewall is shown in Fig. 9a. The strain energy (section *OA*) increases by 426 kJ within 0.023 s, and the σ_θ at measuring circle 1 increases by 69.6 MPa within 0.026 s after tunnel excavation. Therefore, the surface surrounding rock first splits along the joint and moves toward the free surface. At this point, the outermost rock slab is only subjected to σ_θ . If σ_θ continues to increase, the rock slab will be damaged. After failure, the stress rapidly decreases and approaches 0 (measuring circles 1, 2, and 3 in Fig. 11), accompanied by the release of strain energy. There are two types of failure modes. In the first case, the rock slabs bend toward the free surface after compression, and the surrounding rock bulges and then breaks off. In the second case, shear failure occurs in the rock slab, and the tunnel wall is broken and bursts out, accompanied by falling blocks, which is characteristic of a weak rockburst (Gu et al. 2002).

Internal rock mass split into slabs is shown in Fig. 9b, c. When the surface rock mass is damaged, one side of the subsequent rock mass unloads to form a free surface, and σ_θ increases faster (the rate of increase of σ_θ from 1.95 to 2.58 GPa/s at measuring circle 4 in Fig. 11); a larger distance indicates a smaller increase range, resulting in the internal

rock mass being split into slabs along the joint. However, compared with the sidewall, the free surface decreases, and the height of the rock slab with uniaxial compression decreases; the height–diameter ratio of the internal rock slab gradually increases, and the uniaxial compressive strength increases. Furthermore, the radial stress from the excavated surface to the interior of the surrounding rock also gradually increases, and the compressive strength of the surrounding rock increases. When the compressive strength of a certain internal rock mass is larger than σ_θ , the failure zone no longer extends to the interior, such that the final failure zone is V-shaped (Fig. 9). In this stage, the strain energy (section *AB*) fluctuates in a small range.

The internal slab fracture is shown in Fig. 9d. The rock slab gradually breaks down along the surface to the internal rock mass after stratification of the internal rock mass. Rock mass failure occurs at measuring circles 4 and 5, and the stress decreases rapidly, whereas only partial failure occurs at measuring circles 6, 7, and 8, where the residual stress is relatively high. At this state, the strain energy is suddenly released at approximately 117 kJ (section *BC*). Finally, the rock mass gradually fails at each measuring circle; the stress decreases rapidly, and the strain energy accumulated in the failure area is released (section *CD*) with a decrease of approximately 250 kJ. The fracture pattern is similar to that of the first stage.

The rock mass broken up and ejected is shown in Fig. 9e, f. The strain energy accumulated within the failure range is released after the fracture of the rock slab, and the rock slab is gradually broken into blocks after being crushed by the top rock mass and disturbed by internal rock mass destruction. A large amount of kinetic energy is produced, and rock is ejected toward the free surface, causing rockburst.

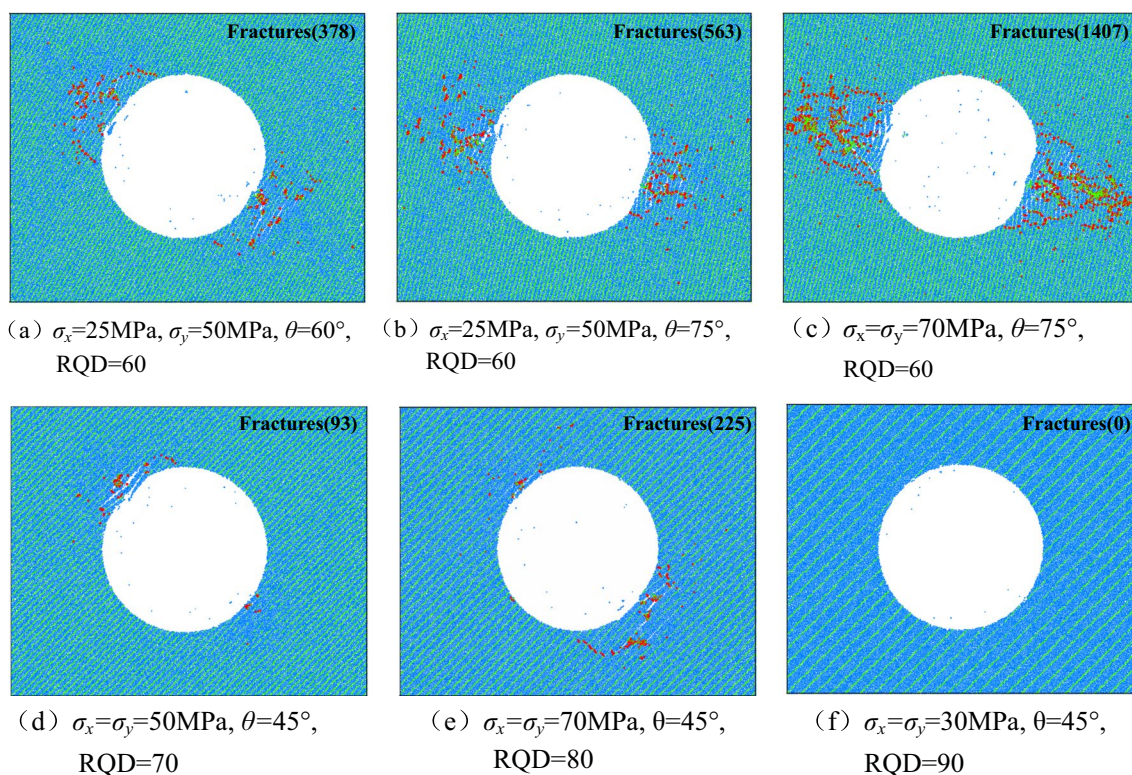


Fig. 12 Failure results under different conditions Note: The green line represents the joint and the red line represents fractures

3.3 Failure results of different types

The damaged area and the degree of damage is shown in Fig. 12. In Fig. 12a–c, the surrounding rock has a large failure area and a high failure degree—it has reached the third stage of rockburst failure. The surrounding rock has been split into slabs and fractured, and numerous particles and a few lumps of rock have been ejected. The maximum velocities V_{\max} of the three cases are 6.40, 8.85, and 9.36 m/s; the maximum kinetic energies KE_{\max} are 80.6, 86.4, and 142.7 kJ, and the kinetic energy differences KE' are 41.4, 47.2, and 39.7 kJ, respectively. Strong rockburst has occurred in all three cases. In Fig. 12d, the first layer of the rock slab is fractured into a block, but there is no internal damage. This represents the first stage of rockburst. The maximum velocity V_{\max} is 8.27 m/s; the maximum kinetic energy KE_{\max} is 66.3 kJ, and the kinetic energy difference KE' is 12.8 kJ, indicating that a weak rockburst has occurred. In Fig. 12e, the surface rock mass of the surrounding rock splits into slabs, but KE' is low. The maximum velocity V_{\max} is 6.06 m/s; the maximum kinetic energy KE_{\max} is 107.8 kJ, and the kinetic energy difference KE' is 4.7 kJ. Spalling damage has occurred. In Fig. 12f, the surrounding rock remains stable, and only a few particles are ejected. The maximum velocity V_{\max} is 1.82 m/s; the maximum kinetic energy KE_{\max} is 23.1 kJ, and the kinetic energy difference

KE' is 4.3 kJ, indicating that no failure has occurred. This also indicates that it is feasible to identify rockbursts from V_{\max} and KE' .

4 Influence of various control factors on rockbursts

4.1 Influence of RQD on Rockbursts

Rock mass quality designation (RQD) is an indicator of rock integrity (Deere 1964). RQD has a great influence on the compressive strength of a rock mass. Gu et al. (2002) noted the important influence of the integrity of surrounding rock on rockbursts in a study of tunnel rockbursts. Therefore, the influence of integrity on tunnel rockbursts is studied by changing the spacing between the joints added in the model.

4.1.1 Influence of RQD on change in tangential stress during rockburst process and kinetic energy at rockburst moment

High stress is one of the most important factors that cause rockburst. The stress in the surrounding rock is redistributed after the disturbance of an excavation. The radial stress decreases, and the tangential stress σ_{θ} increases. When σ_{θ}

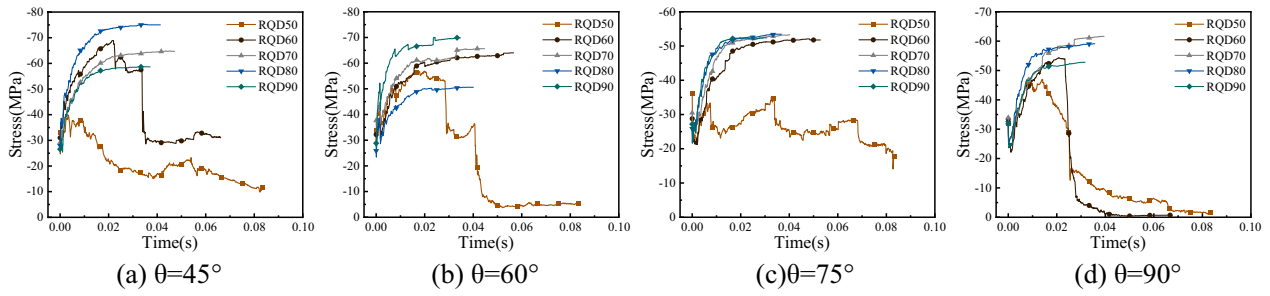


Fig. 13 Tangential stress with different RQD values in the same inclined angles of joints ($\sigma_x = \sigma_y = 30$ MPa)

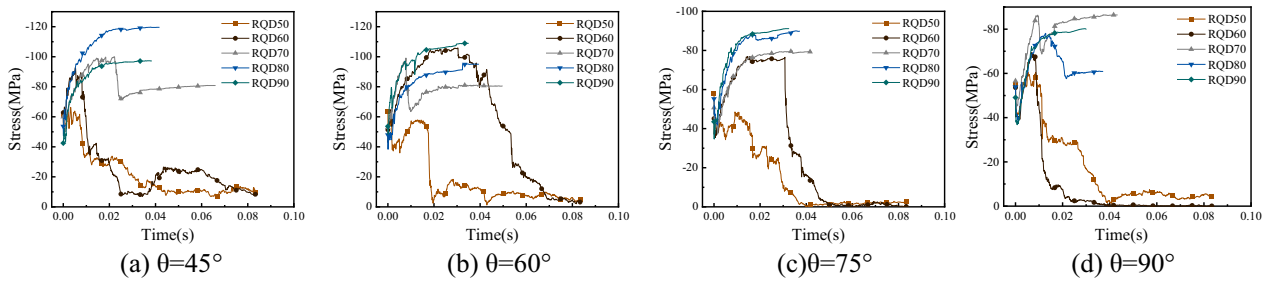


Fig. 14 Tangential stress with different RQD values in the same inclined angles of joints ($\sigma_x = \sigma_y = 50$ MPa)

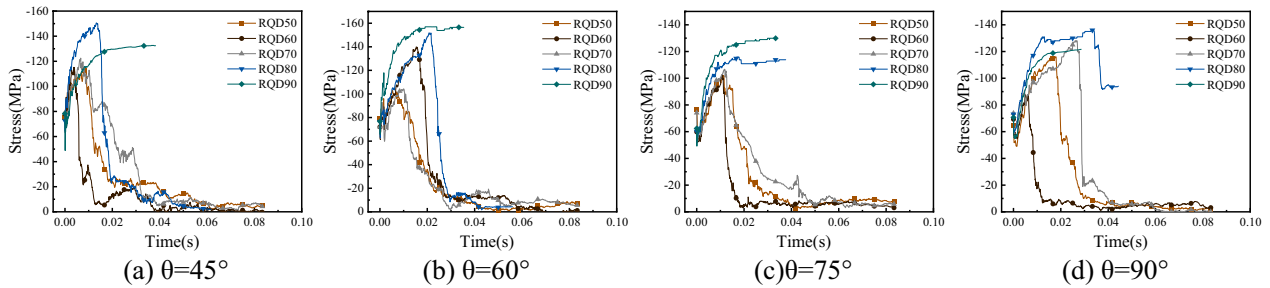


Fig. 15 Tangential stress with different RQD values in the same inclined angles of joints ($\sigma_x = \sigma_y = 70$ MPa)

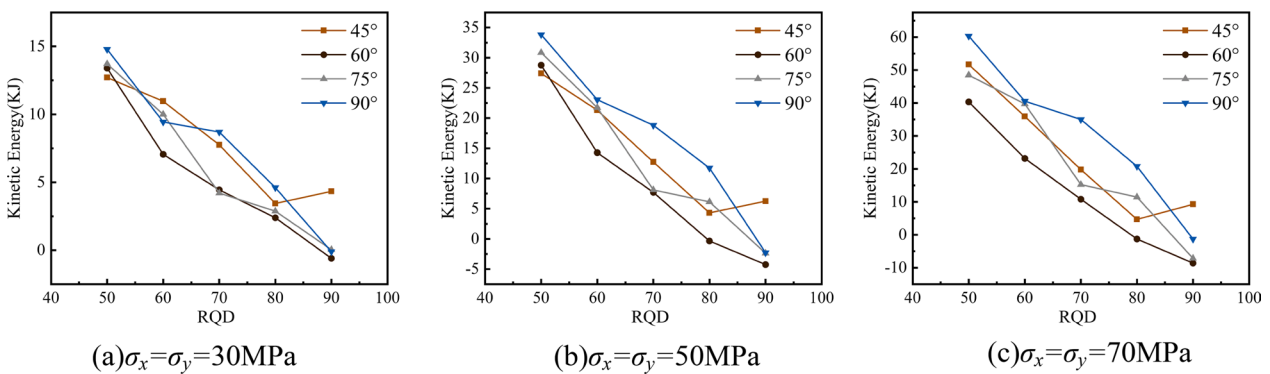


Fig. 16 KE' with different values of θ , RQD and in-situ stress

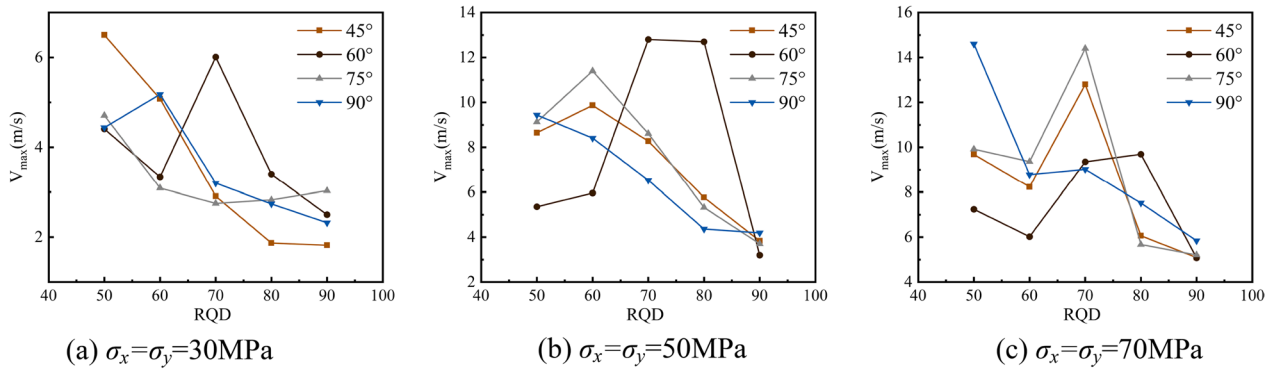


Fig. 17 V_{\max} with different values of θ , RQD and in-situ stress

reaches the bearing limit of the rock mass, the surrounding rock breaks. The accumulated strain energy in the rock mass is rapidly released from the perspective of energy. Part of the strain energy is consumed when the rock mass ruptures. In this process, a small fraction is converted to heat. The remaining energy is converted into kinetic energy, causing the fractured rock mass to eject at a high speed, hence resulting in a rockburst. Studying the change in σ_θ and the magnitude of kinetic energy during a rockburst aids in understanding the characteristics of a rockburst and revealing the rockburst mechanism.

A tunnel excavation usually fails in two places. The position with the largest $\sigma_{\theta\max}$ in these two places is selected for research. Figures 13, 14 and 15 indicate that as the RQD increases, the stress law of σ_θ with changes in time. Figure 14a shows that when $\sigma_x = \sigma_y = 50 \text{ MPa}$ and $\theta = 45^\circ$, with increasing RQD, the shape of the tangential stress curve changes. For RQD = 50, the tangential stress σ_θ increases before the peak stress $\Delta\sigma'_\theta$ reaches 16.6 MPa and decreases after the peak stress $\Delta\sigma''_\theta$ reaches -53.0 MPa within 0.03 s. The residual stress accounts for 15.2% of the peak stress. For RQD = 60, the tangential stress σ_θ increases before the peak stress $\Delta\sigma'_\theta$ reaches 36.6 MPa, and decreases after the peak stress $\Delta\sigma''_\theta$ reaches -84.1 MPa within 0.020 s. The residual stress accounts for 9.1% of the peak stress. For RQD = 70, the tangential stress σ_θ increases before the peak stress $\Delta\sigma'_\theta$ reaches 51.7 MPa and decreases after the peak stress $\Delta\sigma''_\theta$ reaches -28.6 MPa within 0.003 s. The residual stress accounts for 80.8% of the peak stress with increasing RQD, $\Delta\sigma'_\theta$, and the reduction speed of σ_θ after the peak is increased. The reduction speed of σ_θ after the peak likewise improved. The residual stress accounting for the peak stress improves when RQD = 70, indicating that the failure degree of the surrounding rock decreases. When RQD = 80 and 90, the tangential stress σ_θ becomes steady after increasing, which means that the surrounding rock does not fail after excavation. The in situ stress also affects the change law of σ_θ . With increasing in situ stress, $\Delta\sigma'_\theta$ and the reduction

speed of σ_θ increase, while the residual stress accounting for the peak stress decreases at the same RQD and θ . KE' gradually decreases with increasing RQD under the same initial in situ stress condition, and the change law is similar with the same joint inclined angle (Fig. 16). The kinetic energy released during rockburst likewise increases with increasing in situ stress, and the increased amplitude gradually decreases with increasing RQD. The in situ stress increases by 20 MPa each time, and the increment of KE'_{\max} is 19 and 26.5 kJ. With increasing in situ stress, the increase in kinetic energy is nonlinear. This indicates that a lower RQD leads to a higher in situ stress and larger kinetic energy. However, high in situ stress is the fundamental cause of rockburst. The energy accumulated in the surrounding rock is lower under the lower initial ground stress; the kinetic energy released during rockburst is lessened, and no rockburst, or only a weak rockburst occurs.

The measured velocity has several limitations, as the deformation of the rock mass simulated by the discrete element is closer to the discontinuous deformation of the real rock mass. The maximum velocity cannot fully represent the intensity of a rockburst. In this experiment, because the large amount of data and the failure mode are known through the stress change, and the curve of the maximum velocity with the change in RQD shows a high trend in the middle and low on both sides (Fig. 17). This indicates that the kinetic energy of a rockburst is high when RQD is small, but the ejection velocity is low. Therefore, strong ejection-type rockbursts only occur in relatively intact surrounding rocks.

4.1.2 Influence of RQD on Rockburst Failure

The failure range refers to the range of damage and is deducible from the crack propagation area shown in Fig. 18. The failure extent indicates the fragmentation degree of the block in the damaged area. The failure range and extent of the surrounding rock after a rockburst can reflect the destructiveness of the rockburst. Both the failure range and

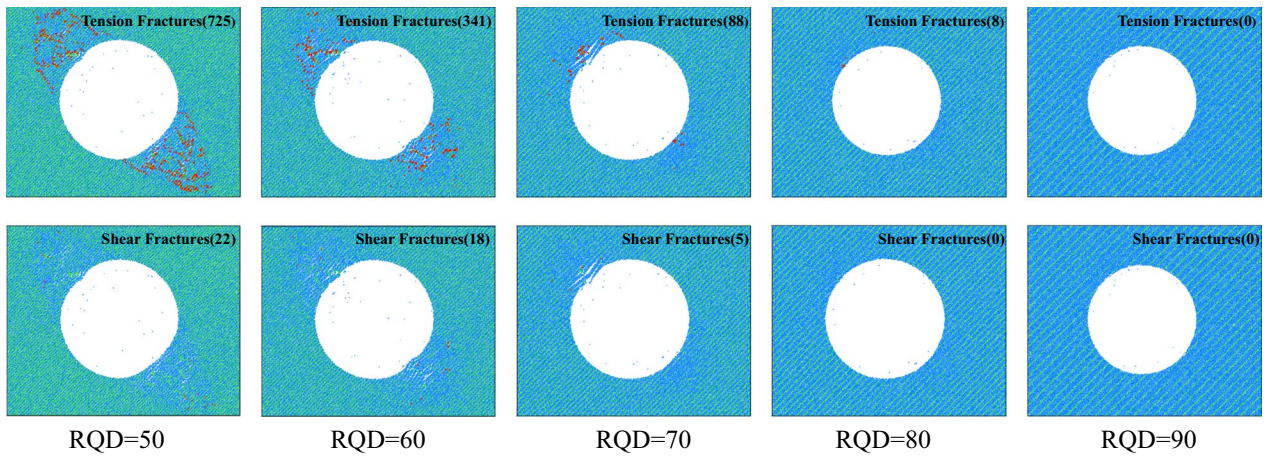


Fig. 18 Failure results of different RQD values (for $\sigma_x = \sigma_y = 50$ MPa and $\theta = 45^\circ$)

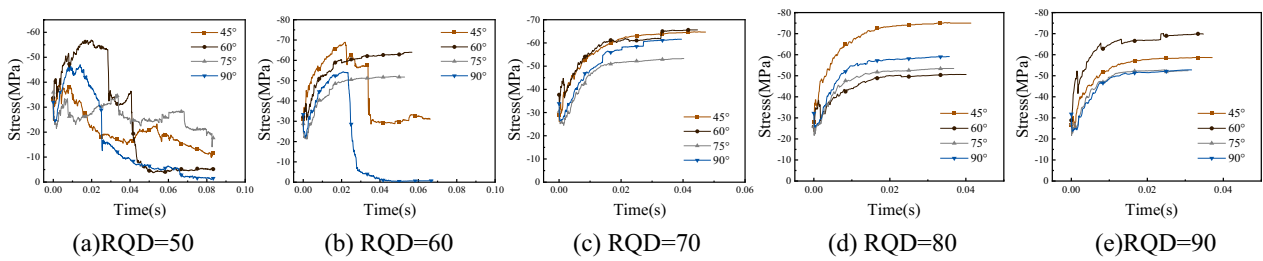


Fig. 19 Tangential stress with different inclined angles of joints in the same RQD ($\sigma_x = \sigma_y = 30$ MPa)

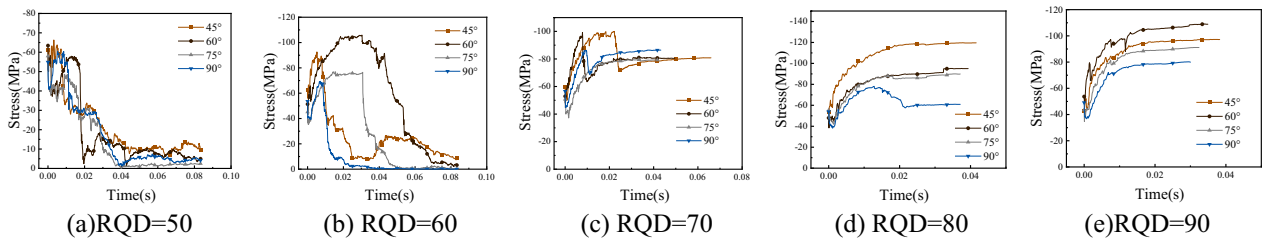


Fig. 20 Tangential stress with different inclined angles of joints in the same RQD ($\sigma_x = \sigma_y = 50$ MPa)

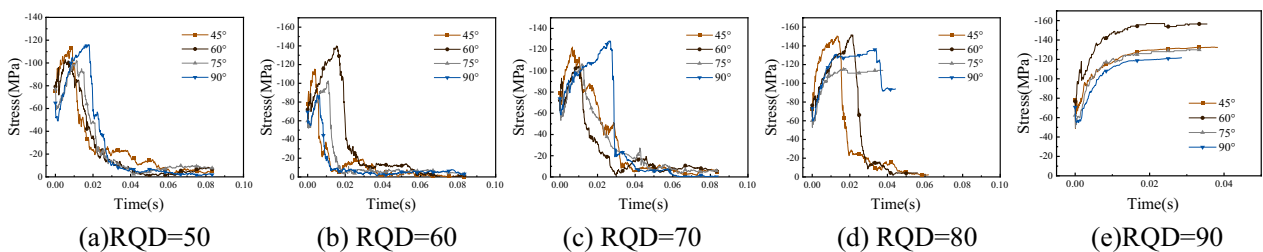


Fig. 21 Tangential stress with different inclined angles of joints in the same RQD ($\sigma_x = \sigma_y = 70$ MPa)

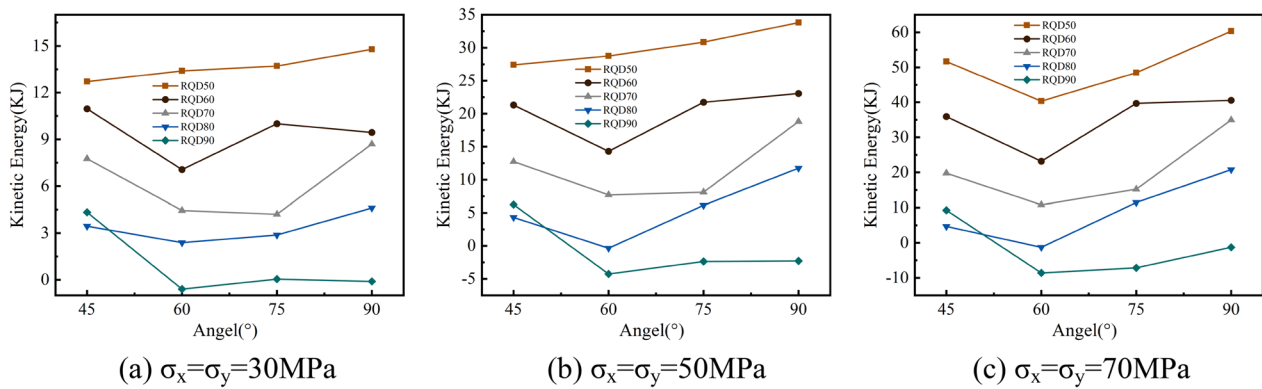


Fig. 22 KE' with different θ , RQD and in-situ stress

the number of crack strips decrease with increasing RQD (Fig. 18). When RQD = 50, the failure range is very large, but only the surface rock on the left sidewall is fractured with $V_{\max} = 8.65 \text{ m/s}$, and the surrounding rock on the right sidewall is split into slabs, but not damaged. The maximum kinetic energy is 27.4 kJ, and medium rockburst occurs. When RQD = 60, the failure range decreases, but the failure degree clearly increases; the failed rocks on the tunnel left sidewall blow out with $V_{\max} = 9.87 \text{ m/s}$, and the internal rock mass splits into slabs. When the maximum kinetic energy is 21.3 kJ, a medium rockburst occurs. At RQD = 70, only the surface of the surrounding rock on the left sidewall breaks out with $V_{\max} = 8.27 \text{ m/s}$. When the maximum kinetic energy is 12.7 kJ, a weak rockburst occurs. At RQD = 80 and RQD = 90, there is little damage to the surrounding rock, and only a few particles are ejected. When the maximum kinetic energies are 4.3 and 6.2 kJ, respectively, no rockburst occurs. Furthermore, the tensile failure of the surrounding rock is far greater than the shear failure. When RQD is small, the range of failure is large, but the extent of failure is small. With the increase in RQD, the range of failure decreases, and the extent of failure increases. The integrity of the surrounding rock likewise has a significant influence on rockbursts. Under the same in situ stress condition, as RQD decreases, the deformation velocity of the surrounding rock increases first, and then decreases. Therefore, a strain burst could occur for joint rock masses at relatively low RQD. Although the ejection speed of this kind of rock burst is relatively low, the volume of the ejected rock block will also increase.

4.2 Influence of joint inclined angle on rockbursts

Studies (He et al. 2021a, b) have shown that the inclined angle of joints in a rock mass is an important factor affecting the mechanical behavior of a rock mass. The change in the inclined angle affects not only the compressive strength of the rock mass, but also the failure mode. As σ_θ in the surrounding rock increases after tunnel excavation, the

surrounding rock cracks in the same direction as the σ_θ expand rapidly and eventually split the rock mass (Gu et al. 2002). Therefore, the inclination angle of the joint contained in the surrounding rock may have a certain influence on a rockburst.

4.2.1 Influence of joint inclined angle on change of tangential stress in rockburst process and kinetic energy during a rockburst

The joint inclined angle only affects whether σ_θ is released and the degree of release in a few cases (Figs. 19b, 20c, d, 21d). This indicates that θ is not the main controlling factor for the failure of the surrounding rock, and only when RQD and induced stress are close to the critical value of a rockburst, will they have a more significant impact. In these cases, the tangential stress release degree decreases first, and then increases as θ increases from 45° to 90°, with the minimum occurring at 75°. In other cases, the joint inclined angle has a significant influence on the stress peak.

As shown in Fig. 22, when RQD = 50 and $\sigma_x = \sigma_y \leq 50 \text{ MPa}$, KE' continues to increase with θ increasing from 45° to 90°. However, KE' decreases first (from 45° to 60°) and then increases at $\sigma_x = \sigma_y = 70 \text{ MPa}$. In other cases, KE' also decreases first (from 45° to 60°) and then increases (from 60° to 90°), with a minimum at $\theta = 60^\circ$ and a maximum at $\theta = 45^\circ$ or 90° . This indicates that, except for RQD and the in situ stress being low (RQD = 50 and $\sigma_x = \sigma_y \leq 50 \text{ MPa}$), as θ increases from 45° to 90°, the rockburst intensity decreases first (from 45° to 60°) and then increases (from 60° to 90°).

4.2.2 Influence of joint inclined angle on rockburst failure

The surrounding rock splits into slabs along the joints and is destroyed perpendicular to them (Fig. 23). The failure mode is mostly tensile failure and less shear failure. Tensile failure mostly occurs at the edge of the failure area and the splitting

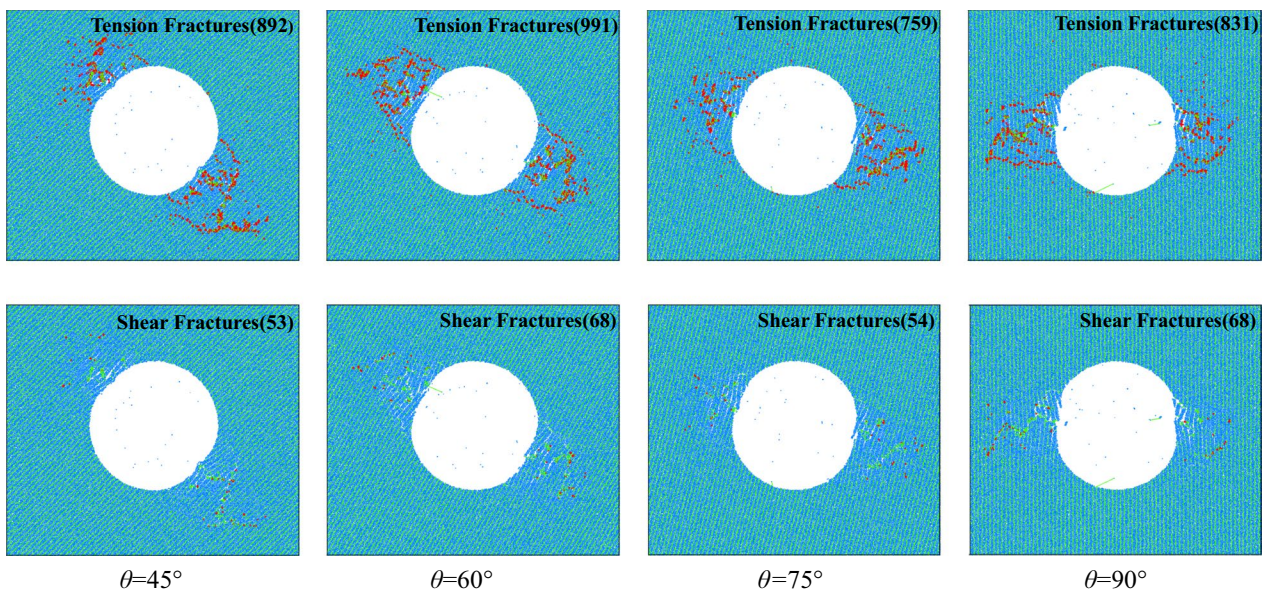


Fig. 23 Failure results of different joint inclination angles (for $\sigma_x = \sigma_y = 70$ MPa and RQD = 70)

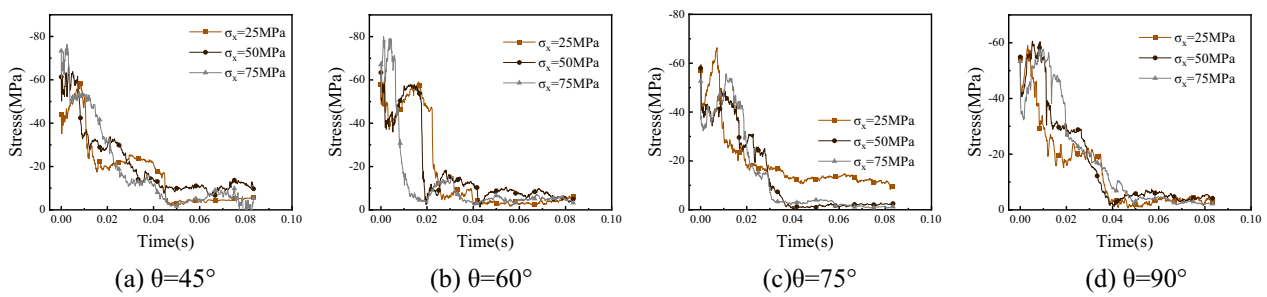


Fig. 24 Tangential stress with different σ_x in the same inclined angles of joints (RQD = 50)

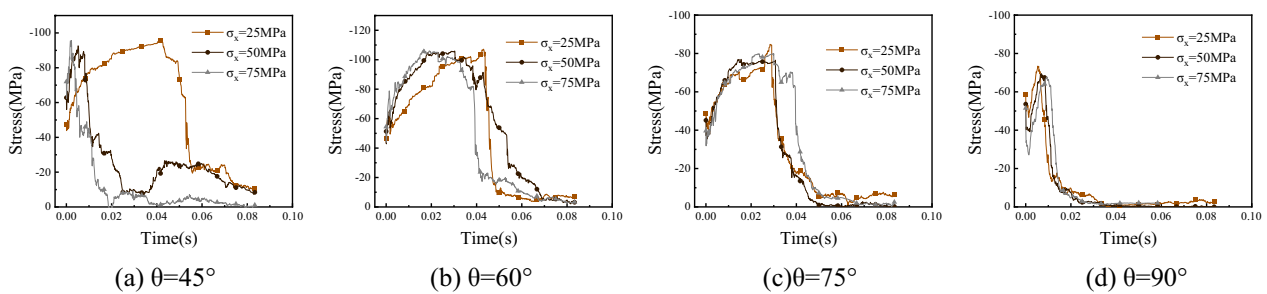


Fig. 25 Tangential stress with different σ_x in the same inclined angles of joints (RQD = 60)

and breaking of the surface rock slab, while shear failure mostly occurs at the internal rock slab. Moreover, when $\theta = 45^\circ$, the surface of the surrounding rock only undergoes a bending uplift. With increasing θ , when $\theta = 90^\circ$, some large blocks are ejected, and part of the surface rock mass

will fracture into blocks and be completely separated from the surrounding rock. θ is the main controlling factor of the rockburst position, and with θ increasing from 45° to 90° , the damage degree of the surrounding rock increases slightly. Because the position of rockburst is always perpendicular to

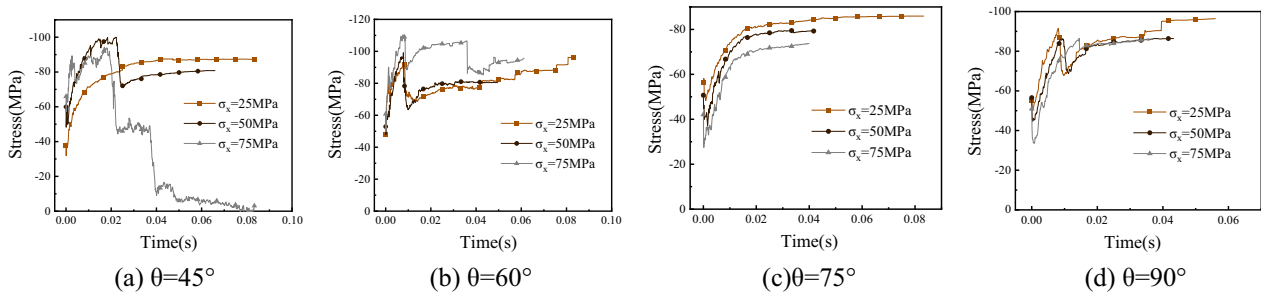


Fig. 26 Tangential stress with different σ_x in the same inclined angles of joints (RQD = 70)

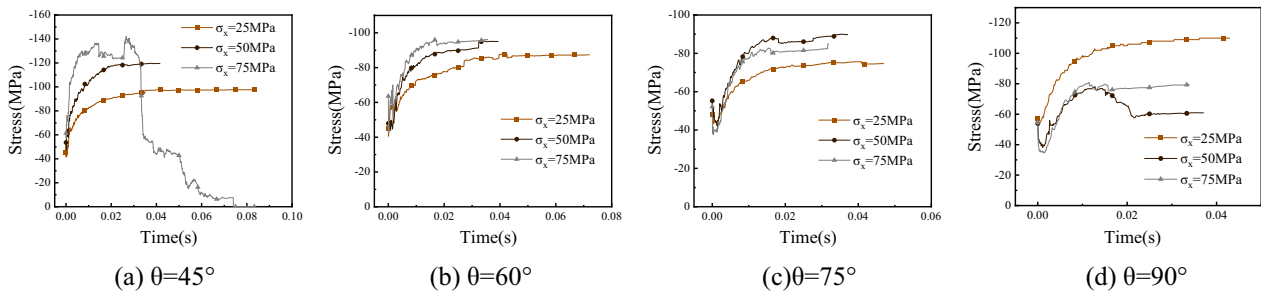


Fig. 27 Tangential stress with different σ_x in the same inclined angles of joints (RQD = 80)

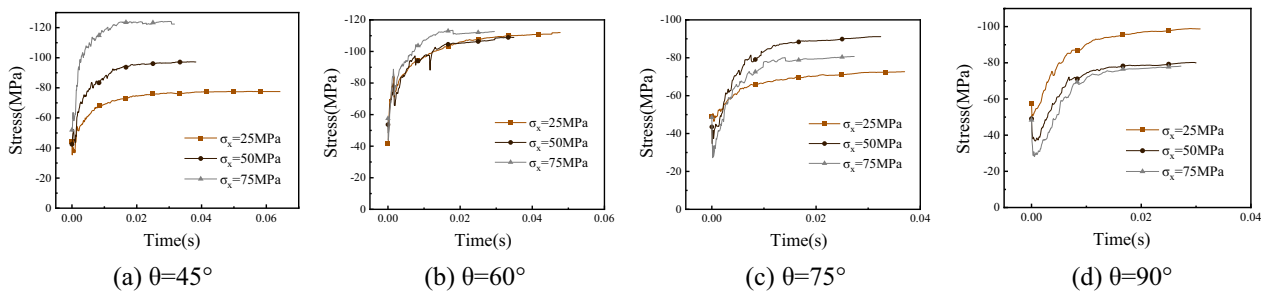


Fig. 28 Tangential stress with different σ_x in the same inclined angles of joints (RQD = 90)

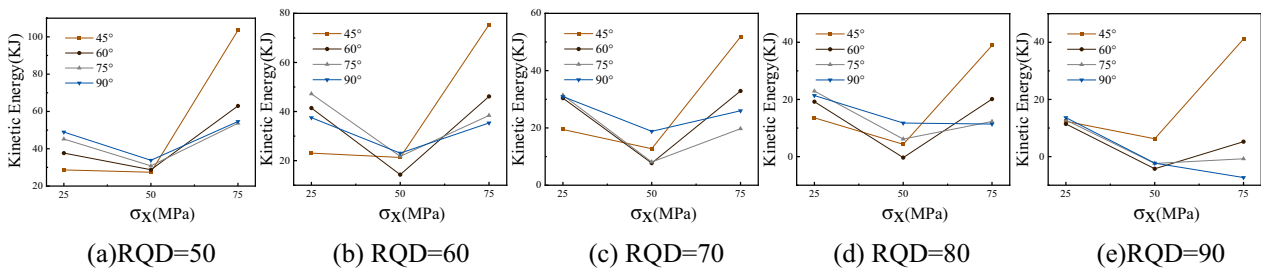


Fig. 29 KE' with different values of θ , RQD and σ_x

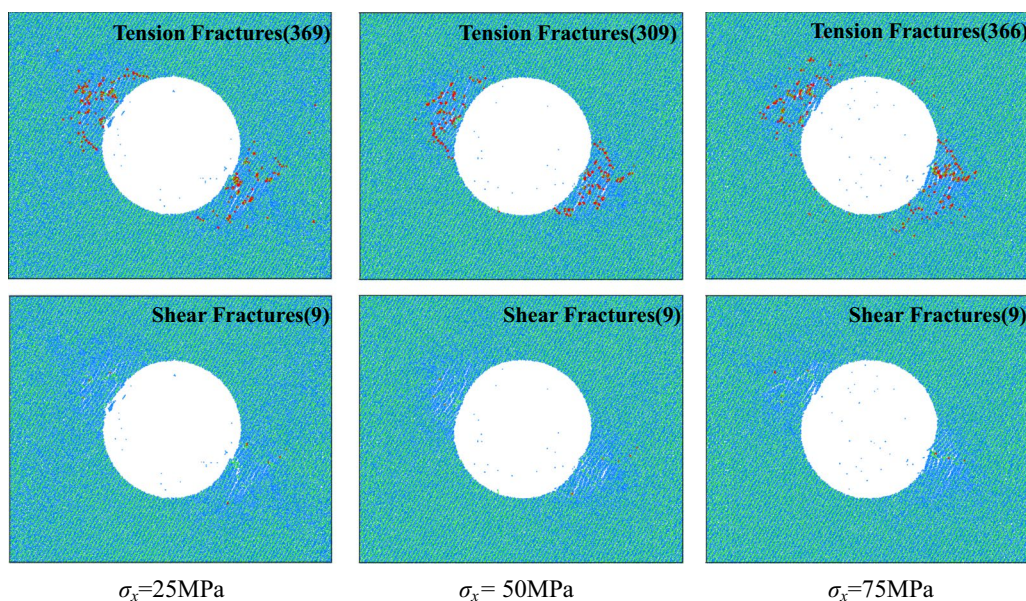


Fig. 30 Failure results under different σ_x (for $\sigma_y=50$ MPa, RQD=60 and $\theta=60^\circ$)

the joint, it can be considered that the angle between tangential stress and the joint at the failure location is small. Therefore, when $\sigma_x = \sigma_y$, the change in θ mainly affects the position of the rockburst, and it is not the main controlling factor of the occurrence and intensity of the rockburst.

4.3 Influence of lateral pressure on rockburst

4.3.1 Influence of lateral pressure on change in tangential stress during rockburst process and kinetic energy at time of rockburst

When RQD is relatively small (RQD = 50 and 60), the compressive strength of the rock mass is low. The change in lateral pressure σ_x mainly affects the time required for σ_θ to reach peak stress (Figs. 24, 25); when $\theta=45^\circ$, a larger

σ_x requires a shorter time, and vice versa. With increasing RQD, the influence of σ_x is gradually reflected in $\sigma_{\theta\max}$ (Figs. 26, 27, 28). When $\theta=45^\circ$ and 60° , a larger σ_x leads to a larger $\sigma_{\theta\max}$. When $\theta=75^\circ$, with increasing σ_x , the minimum of σ_θ occurs at $\sigma_x=25$ MPa, and the maximum of σ_θ occurs at $\sigma_x=50$ MPa. When $\theta=90^\circ$, the maximum of σ_θ occurs at $\sigma_x=25$ MPa, and the minimum of σ_θ occurs at $\sigma_x=75$ MPa.

The change in kinetic energy KE' with the lateral stress σ_x shows a trend of first decreasing and then increasing (Fig. 29), and the law is related to θ and RQD. When $\theta=45^\circ$, $RQD \leq 60$, and with increasing σ_x , KE' remains unchanged (from 25 to 50 MPa), and then increases (from 50 to 75 MPa). When $\theta=90^\circ$ and $RQD \geq 80$, KE' continues to decrease as σ_x increases. In other cases, KE' first

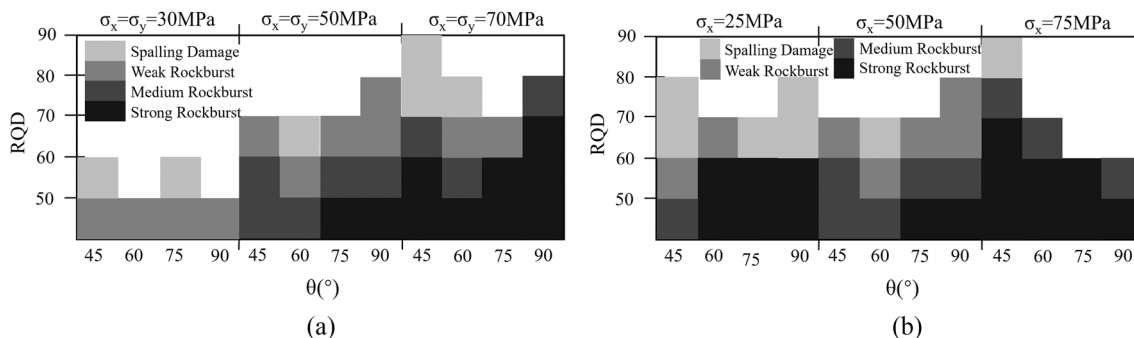


Fig. 31 Classification results

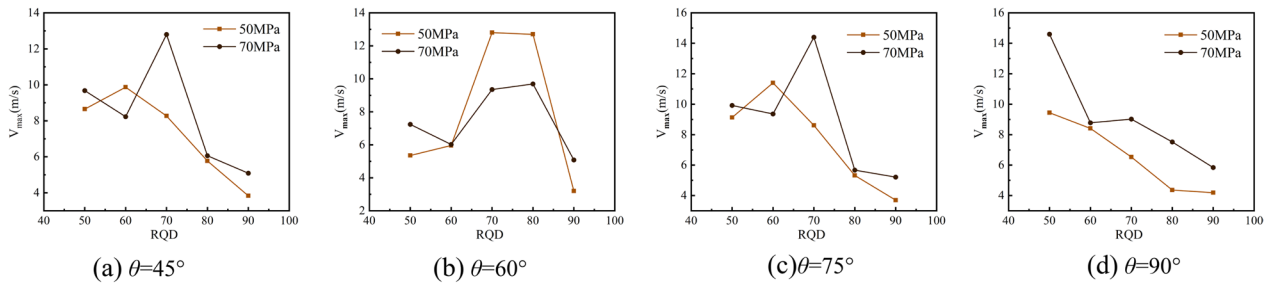


Fig. 32 V_{max} with different RQD and in-situ stress values in the same θ

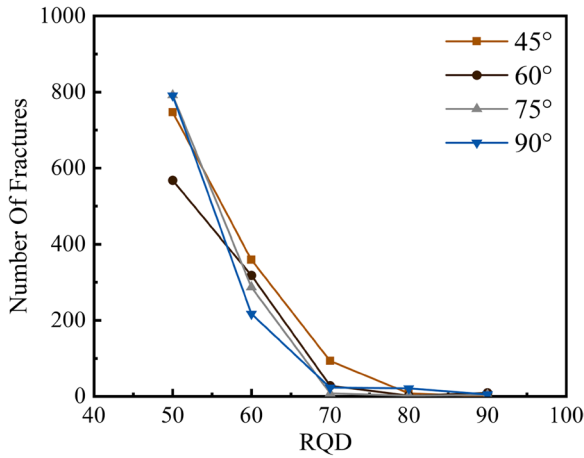


Fig. 33 Number of cracks with different RQD and θ when $\sigma_x = \sigma_y = 50$ MPa

decreases and then increases, with the minimum occurring at $\sigma_x = 50$ MPa.

4.3.2 Influence of lateral pressure on rockburst failure

When $\sigma_x = 25$ MPa, the surface of the surrounding rock is fractured, the internal rock mass is split into slabs, and some rock blocks are ejected with $V_{max} = 6.4$ m/s (Fig. 30). When the maximum kinetic energy is 41.4 kJ, a strong rockburst occurs. At $\sigma_x = 50$ MPa, the damage of the surrounding rock is reduced. The KE' is low ($KE' = 14.3$ kJ), and no larger blocks are ejected. When the maximum velocity is 5.9 m/s, a weak rockburst occurs. At $\sigma_x = 75$ MPa, the rock mass on the right sidewall is broken into blocks, and the blocks blow out with $V_{max} = 7.47$ m/s. When the maximum kinetic energy is 46.2 kJ, a strong rockburst occurs. This indicates that increasing (from 50 to 75 MPa) or decreasing (from 50 to 25 MPa) the lateral pressure σ_x can increase the intensity of a rockburst. When $\sigma_x < \sigma_y$, the intensity of the rockburst decreases with increasing σ_x ; when $\sigma_x = \sigma_y$, the rockburst intensity is the lowest; when $\sigma_x > \sigma_y$, the intensity of the rockburst increases with increasing σ_x .

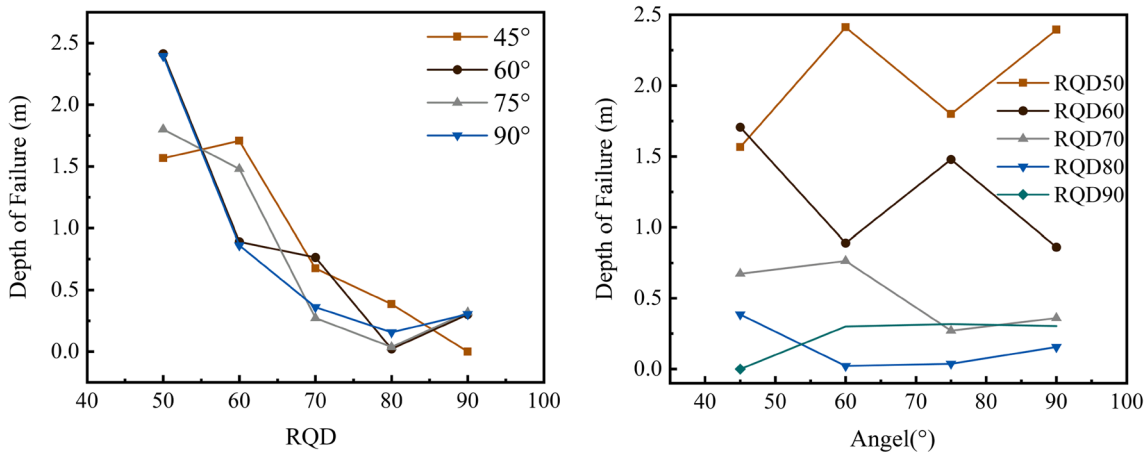


Fig. 34 Depth of failure with different θ , RQD values (for $\sigma_x = \sigma_y = 50$ MPa)

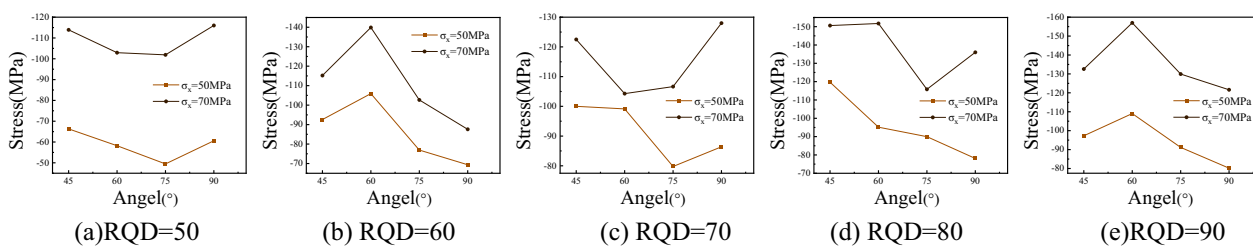


Fig. 35 Peak stress with different θ and in-situ stress values in the same RQD

5 Discussion and conclusions

Currently, research on rockburst processes is mostly based on field observations (Gu et al. 2002; Tan 1989) or laboratory tests (Gong et al. 2018a, b). These methods are highly effective, however, it is difficult to study the deformation characteristics, stress, and strain energy changes inside the surrounding rock during a rockburst event. In this study, PFC2D is used to simulate the excavation of a layered jointed surrounding rock tunnel, and the entire process from excavation to rockburst is obtained (Fig. 9). The σ_θ in the surrounding rock increases after excavation, and the increase rate of the σ_θ is faster the closer it is to the free surface. Moreover, the σ_θ inside the surrounding rock is increased after the failure of the rock mass near the free surface, and the increase rate of stress is faster, showing a form of layered failure from the sidewall to the interior. The compressive strength of the rock mass gradually increases with decreasing free surface area. Combined with the evolution law of strain energy during the rockburst process, and the deformation characteristics of the surrounding rock inside and outside, the rockburst of the layered jointed tunnel can be divided into four stages: slab buckling of the tunnel sidewall, internal rock mass splitting into slabs, internal slab fracture, and rock mass breakup and ejection.

Yeung and Leong (1997) used the discontinuous deformation analysis (DDA) model to simulate the excavation of horseshoe tunnels with cross joints and studied the influence of joint inclination and spacing on rockbursts. However, most simulated results ended in slippage failure, and they did not provide the effect of joint inclined angles and spacing on the ejection velocity and kinetic energy release analysis. In this study, the changes in stress, ejection velocity, and kinetic energy of the surrounding rock are combined with the failure results of the surrounding rock, and a more detailed study is conducted. First, KE' is compared with the failure results of the surrounding rock, and the results of 100 groups of numerical simulation tests are classified. When $\sigma_x = \sigma_y$, the results are classified according to Eq. (4).

$$\begin{cases} KE' \leq 10 & \text{No Rockburst} \\ 10 < KE' \leq 20 & \text{Weak Rockburst} \\ 20 < KE' \leq 30 & \text{Medium Rockburst} \\ 30 < KE' & \text{Strong Rockburst} \end{cases} \quad (4)$$

When $\sigma_y = 50$ MPa, $\sigma_x = 25$ and 75 MPa, the change in lateral pressure leads to an increase in the number of particles flying out of the tunnel wall (Fig. 30), which significantly increases the measured kinetic energy. However, there is no corresponding degree of damage inside the surrounding rock. Equation 6 must be modified, so when $\sigma_x \neq \sigma_y$, it is classified according to Eq. (5).

$$\begin{cases} KE' \leq 20 & \text{No Rockburst} \\ 20 < KE' \leq 25 & \text{Weak Rockburst} \\ 25 < KE' \leq 35 & \text{Medium Rockburst} \\ 35 < KE' & \text{Strong Rockburst} \end{cases} \quad (5)$$

When KE' is relatively small, there are still some surrounding rocks with delamination failure, but the deformation velocity is relatively small, such that it can be considered that spalling damage occurs. The classification results are shown in Fig. 31.

The occurrence and intensity of rockburst are mainly determined by the quantity and release rate of energy during failure of the surrounding rock. According to Fig. 10b, all strain energy accumulated in the surrounding rock after excavation was released during the rockburst. The magnitude of the released energy can be considered equal to the magnitude of the strain energy accumulated in the surrounding rock after excavation disturbance. Moreover, the accumulated strain energy is released suddenly after the rock mass has broken to a certain extent. The released strain energy W_e is converted into other energy after the rockburst, as shown in Eq. (6) (Charlie 2021).

$$W_e = W_f + W_k + W_v \quad (6)$$

where, W_e is the strain energy; W_f is the energy consumed by rock fracture; W_k is the kinetic energy of the ejected rock, and W_v is the thermal, vibration and other energy generated

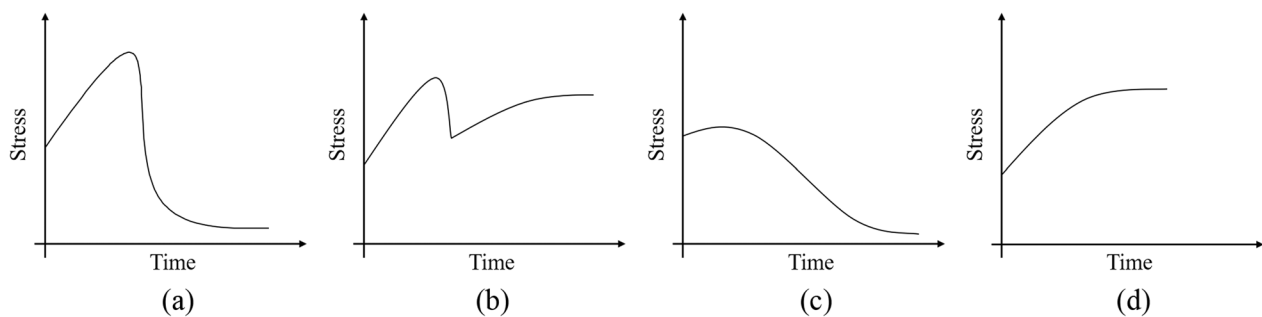


Fig. 36 Different types of stress curves with time

during the rockburst process. After obtaining the rockburst intensity under various conditions, the occurrence conditions of rockburst under the same rock conditions can be simply analyzed as follows:

(1) Integrity

The tunnel surrounding the rock is a carrier of energy storage, and the more complete the rock is, the higher the energy W_f consumed by failure will be. Figure 31 shows that under the same joint inclined angle θ and initial in situ stress, a smaller RQD indicates that a rockburst is more likely to occur, leading to larger rockburst intensity. In this process, the change in W_e is small under the same conditions, while W_v only accounts for a small part. Thus, W_f decreases in the process of decreasing RQD, resulting in an increase in W_k and a more violent rockburst. However, previous studies found that the σ_θ and kinetic energy changes at RQD 50 are different from those at RQD > 50. When $\sigma_x = \sigma_y$, the maximum deformation velocity of the surrounding rock is analysed (Fig. 32). Because only weak rockburst occurs, this is not considered when $\sigma_x = \sigma_y = 30$ MPa.

When $\theta = 45^\circ, 60^\circ$, and 75° , the maximum deformation velocity of the surrounding rock has a turning point between RQD 50 and 70 (Fig. 32). After the turning point, as RQD decreases, the deformation velocity of the surrounding rock gradually decreases. The maximum distance between the fractures generated by the failure and the sidewall is defined as the depth of failure. The depth of failure gradually decreases with increasing RQD. Because the failure range of the surrounding rock increases exponentially (Figs. 18, 33, 34), the unit kinetic energy decreases, and the deformation rate of the surrounding rock decreases, although the overall kinetic energy increases at the time of failure. This indicates that there must be a threshold value of RQD, below which the deformation velocity is very small, and the failure of the surrounding rock is no longer a rockburst. However, when $\theta = 90^\circ$, the deformation velocity of the surrounding rock continues to increase with decreasing RQD. Evidently, the inclined angle of the joint has a certain influence on it.

The change in the kinetic energy during rockburst with θ is given in Fig. 22. The kinetic energy of the rockburst first decreases, and then increases with the inclination of the joint from 45° to 90° , and it is the smallest at 60° .

Figure 35 shows that the influence of the joint inclined angle on the stress peak is still related to RQD. When rockbursts (RQD 50 and 60) or no rockbursts (RQD 90) occur in the surrounding rocks, the stress peak value changes with the joint inclination angle. Only when RQD = 60 does the rock mass in the measuring circle completely undergo brittle failure. According to Fig. 35b, the compressive strength of the rock mass increases first and then decreases, reaching a maximum at 60° , while the rockburst intensity decreases first and then increases, reaching a minimum at 60° . Thus, when RQD ≥ 60 , the higher the compressive strength of the rock mass leads to a lower rockburst intensity.

(2) In situ stress

The initial in situ stress is the source of energy in the surrounding rock, and its magnitude directly determines the magnitude of W_e in the rock mass. When $\sigma_x = \sigma_y$, as the in situ stress increases, the intensity of rockburst occurring at the same RQD and the inclined angle increase (Fig. 31a). This demonstrates that the strain energy W_e increases with increasing in situ stress. When $\sigma_x \neq \sigma_y$, the damage degree of the surrounding rock increases, and the number of particles ejected from the cave wall increases (Fig. 30). Compared with $\sigma_x = \sigma_y$, the rockburst intensity increases significantly (Fig. 31b). According to the Kirsh solution, for a circular cavity, the maximum shear stress around the cavity appears in the direction parallel to the maximum principal stress, and its value is $3\sigma_1 - \sigma_3$. The minimum shear stress is in the direction parallel to the minimum principal stress, and its value is $3\sigma_3 - \sigma_1$. When σ_x is less than σ_y , assuming that σ_y is the maximum principal stress and σ_x is the minimum principal stress, the circumferential stress increases gradually with θ from 45° to 90° . When $\sigma_x > \sigma_y$, assuming that σ_x is the maximum principal stress and σ_y is the minimum principal stress, the circumferential stress decreases gradually with θ from

45° to 90° (Fig. 35). This is similar to the distribution pattern of rockburst occurrence and intensity shown in Fig. 31b.

(3) Energy release rate

By observing the change rule of σ_θ for the rock mass at the failure position during a rockburst, the change curve of stress with time can be divided into the following four types (Fig. 36). According to the combination of the rate of stress reduction and the failure kinetic energy, the ejection velocity, and failure results corresponding to these four types of stress–time curves, three surrounding rock deformation modes corresponding to these four changing laws are obtained:

- (a) σ_θ gradually increases after the tunnel is excavated. The rock mass is destroyed after the compressive strength of the rock mass is exceeded, and the stress suddenly drops sharply. At this time, there two scenarios are possible. The residual stress is extremely low, which means that all the rock masses within the range of the measurement circle are damaged, the bearing capacity is completely lost, the kinetic energy is large, the failure range is large, and the ejection speed is high.
- (b) The residual stress is high and may continue to grow, which means that only part of the rock mass in this range has failed, while the bearing capacity has not been completely lost. Hence, after part of the rock mass is split into slabs, only bending deformation or surface rock mass fracture occurs. These two stress curves can distinguish the rockburst intensity according to the magnitude of the instantaneous release of the stress.
- (c) After σ_θ increases slightly, the surrounding rock gradually breaks, and the stress releases slowly, indicating that the stored energy inside the rock mass releases slowly. This is more common when the ground stress is low, and the surrounding rock is more broken. As shown in Fig. 13a, c, weak rockburst occurs.
- (d) σ_θ in the surrounding rock of the tunnel increases, but does not exceed the compressive strength of the rock mass. After the increase, it gradually stabilizes. A small number of particles may be ejected, and the surrounding rock does not break.

The stress release process represented by the type (a), (b), (c) and (d) curves in Fig. 36 is a necessary condition for the occurrence of high-speed ejection-type strong rockburst.

Acknowledgements This study was sponsored by the National Natural Science Foundation of China (Grants Nos. 42177158, 11902249 and 11872301), Natural Science Foundation of Shaanxi Province (Shaanxi Province Natural Science Foundation) (Grant No. 2022SF-412) and Education Bureau of Shaanxi Province | Scientific Research

Plan Projects of Shaanxi Education Department in China (Grant No. 20JS093). The financial support provided by this sponsor is greatly appreciated.

Declarations

Conflict of interest The authors declare no conflict of interest.

Open Access This article is licensed under a Creative Commons Attribution 4.0 International License, which permits use, sharing, adaptation, distribution and reproduction in any medium or format, as long as you give appropriate credit to the original author(s) and the source, provide a link to the Creative Commons licence, and indicate if changes were made. The images or other third party material in this article are included in the article's Creative Commons licence, unless indicated otherwise in a credit line to the material. If material is not included in the article's Creative Commons licence and your intended use is not permitted by statutory regulation or exceeds the permitted use, you will need to obtain permission directly from the copyright holder. To view a copy of this licence, visit <http://creativecommons.org/licenses/by/4.0/>.

References

- Amin M, Cai M (2018) Numerical modeling of rockburst near fault zones in deep tunnels. *Tunn Undergr Space Technol* 80:164–180. <https://doi.org/10.1016/j.tust.2018.06.015>
- Cai M (2013) Principles of rock support in burst-prone ground. *Tunn Undergr Space Technol* 36:46–56. <https://doi.org/10.1016/j.tust.2013.02.003>
- Charles H, Dowding C-A (1986) Potential for rockbursting and slabbing in deep caverns. *Eng Geol* 22(3):265–279
- Charlie CL (2021) Principles and methods of rock support for rockburst control. *J Rock Mech Geotech Eng* 13(1):46–59. <https://doi.org/10.1016/j.jrmge.2020.11.001>
- Chen B (2020) Stress-induced trend: the clustering feature of coal mine disasters and earthquakes in China. *Int J Coal Sci Technol* 7(4):676–692. <https://doi.org/10.1007/s40789-020-00334-z>
- Chen ZH, Tang CA, Huang RQ (1997) A double rock sample model for rockbursts. *Int J Rock Mech Min Sci* 34:991–1000
- Chen GQ, Li TB, Zhang GF, Yin HY, Zhang H (2014) Temperature effect of rock burst for hard rock in deep-buried tunnel. *Nat Hazards* 72:915–926. <https://doi.org/10.1007/s11069-014-1042-6>
- Chen YL, Zuo JP, Liu DJ, Li YJ, Wang ZB (2021) Experimental and numerical study of coal-rock bimaterial composite bodies under triaxial compression. *Int J Coal Sci Technol* 8:908–924
- Cheng JL, Sun XY, Feng L, Yuan YB (2012) Experimental study on non-destructive testing of rock bolts based on pseudo-random signal. *Safety Sci* 50(4):783–786
- Christopher M (2016) Coal bursts in the deep longwall mines of the United States. *Int J Coal Sci Technol* 3:1–9
- Deere DU (1964) Technical description of rock cores for engineering purposes. *Rock Mech Rock Eng* 1(1):16–22
- Dou LT, Yang K, Chi XL (2021) Fracture behavior and acoustic emission characteristics of sandstone samples with inclined pre-cracks. *Int J Coal Sci Technol* 8(1):77–87. <https://doi.org/10.1007/s40789-020-00344-x>
- Feng GL, Feng XT, Chen BR et al (2015) A microseismic method for dynamic warning of rockburst development processes in tunnels. *Rock Mech Rock Eng* 48(5):2061–2076
- Feng GL, Feng XT, Chen BG et al (2019) Effects of structural planes on the microseismicity associated with rockburst development

- processes in deep tunnels of the Jinping-II Hydropower Station, China. *Tunn Undergr Space Technol* 84:273–280. <https://doi.org/10.1016/j.tust.2018.11.008>
- Feng GL, Chen BR, Jiang Q et al (2021) Excavation-induced microseismicity and rockburst occurrence: similarities and differences between deep parallel tunnels with alternating soft-hard strata. *J Cen South Univ* 28:582–594. <https://doi.org/10.1007/s11069-014-1042-6>
- Gao HK, Wang Q, Jiang B, Zhang P, Jiang ZH, Wang Y (2021) Relationship between rock uniaxial compressive strength and digital core drilling parameters and its forecast method. *Int J Coal Sci Technol* 8(4):605–613. <https://doi.org/10.1007/s40789-020-00383-4>
- Gong FQ, Luo Y, Li XB, Si XF, Tao M (2018a) Experimental simulation investigation on rockburst induced by spalling failure in deep circular tunnels. *Tunn Undergr Space Technol* 81(81):413–427. <https://doi.org/10.1016/j.tust.2018.07.035>
- Gong FQ, Si XF, Li XB, Wang SY (2018b) Experimental investigation of strain rockburst in circular caverns under deep three-dimensional high-stress conditions. *Rock Mech Rock Eng* 52:1459–1474. <https://doi.org/10.1016/j.tust.2018.11.008>
- Gong FQ, Yan JY, Li XB, Luo S (2019) A peak-strength strain energy storage index for rock burst proneness of rock materials. *Int J Rock Mech Min Sci* 117:76–89. <https://doi.org/10.1016/j.ijrmms.2019.03.020>
- Gong FQ, Luo S, Lin G, Li XB (2020) Evaluation of shear strength parameters of rocks by preset angle shear, direct shear and triaxial compression tests. *Rock Mech Rock Eng*. <https://doi.org/10.1007/s00603-020-02050-1>
- Gu MC, He FL, Chen CZ (2002) Study on rockburst in qingling tunnel. *CJRME* 21(9):1324–1329
- He MC, Li JY, Ren FQ (2020) Rock burst criterion based on clay mineral content. *Arab J Geosci* 13:185. <https://doi.org/10.1016/j.ijrmms.2019.03.020>
- He MM, Zhang ZQ, Zhu JW, Li N, Li GF, Chen YS (2021a) Correlation between the rockburst proneness and friction characteristics of rock materials and a new method for rockburst proneness prediction: Field demonstration. *J Pet Sci Eng* 205:108997. <https://doi.org/10.1016/j.petrol.2021.108997>
- He MC, Li JY, Ren FQ, Liu DQ (2021b) Experimental investigation on rockburst ejection velocity of unidirectional double-face unloading of sandstone with different bedding angles. *CJRME* 40(03):433–447
- Hedley DGF (1992) *Rockburst handbook for Ontario Hardrock Mines*. Energy, Mines and Resources Canada, Canada Center for Mineral and Energy Technology
- Huan JY (2021) Research of macro and micro mechanism of shear strength and quantitative description of 3D roughness for rock joints. Dissertation, Xi'an University of Technology
- Itasca Consulting Group Inc. (2016) *PFC2D manual*, version 5.0 Minneapolis, Minnesota
- Jian Z, Li XB, Shi XZ (2012) Long-term prediction model of rockburst in underground openings using heuristic algorithms and support vector machines. *Saf Sci* 50(4):629–644. <https://doi.org/10.1016/j.ssci.2011.08.065>
- Jiang Q, Feng XT, Xiang TB, Su GS (2010) Rockburst characteristics and numerical simulation based on a new energy index: a case study of a tunnel at 2,500 m depth. *Bull Eng Geol Environ* 69:381–388. <https://doi.org/10.1007/s10064-010-0275-1>
- Jiang Q, Su GS, Feng XT, Cui J, Pan PZ, Jiang JQ (2015) Observation of rock fragment ejection in post-failure response. *Int J Rock Mech Min Sci*. <https://doi.org/10.1016/j.ijrmms.2014.11.007>
- Jiang R, Dai F, Liu Y, Li A (2021a) Fast marching method for microseismic source location in caverncontaining rockmass: performance analysis and engineering application. *Engineering*. <https://doi.org/10.1016/j.eng.2020.10.019>
- Jiang R, Dai F, Liu Y, Li A, Feng P (2021b) Frequency characteristics of acoustic emissions induced by crack propagation in rock tensile fracture. *Rock Mech Rock Eng* 54:2053–2065. <https://doi.org/10.1007/s00603-020-02351-5>
- John H, Kamran E, Martin G (2009) Stability analysis of vertical excavations in hard rock by integrating a fracture system into a PFC model. *Tunn Undergr Space Technol* 24(3):296–308. <https://doi.org/10.1016/j.ijrmms.2014.11.007>
- Kaiser PK, Cai M (2012) Design of rock support system under rockburst condition. *J Rock Mech Geotech Eng* 4(3):215–227
- Kaiser P, McCreath D, Tannant D (1996) *Rockburst support handbook*. Geomechanics Research Centre, Laurentian University, Canada
- Kias E, Ozbay U (2013) Modeling unstable failure of coal pillars in underground mining using the discrete element method. In: 47th US Rock Mechanics/Geomechanics Symposium. American Rock Mechanics Association p. Paper 165
- Lee SM, Park BS, Lee SW (2004) Analysis of rockbursts that have occurred in a waterway tunnel in Korea. *Int J Rock Mech Min Sci* 41:911–916
- Leger JP (1991) Trends and causes of fatalities in South African mines. *Saf Sci* 14(3–4):169–185
- Mansurov V (2001) Prediction of rockbursts by analysis of induced seismicity data. *Int J Rock Mech Min Sci* 38:893–901
- Paige ES, Laurent G, Stephen DM (2013) The role of geologic structure and stress in triggering remote seismicity in Creighton Mine, Sudbury, Canada. *Int J Rock Mech Min Sci* 58:166–179. <https://doi.org/10.1016/j.ijrmms.2014.11.007>
- Potyondy DO, Cundall PA (2004) A bonded-particle model for rock. *Int J Rock Mech Min Sci* 41:1329–1364
- Priest SD, Hudson J (1976) Discontinuity spacing in rock. *Int. J. Rock Mech. Min. Sci. Geomech. Abstr.* 13(5):135–148
- Qiu JD, Luo L, Li XB, Li DY, Chen Y, Luo Y (2020a) Numerical investigation on the tensile fracturing behavior of rock-shotcrete interface based on discrete element method. *Int J Min Sci Technol* 30(3):293–301. <https://doi.org/10.1016/j.ijmst.2020.03.007>
- Qiu JD, Li DY, Li XB, Zhu QQ (2020b) Numerical investigation on the stress evolution and failure behavior for deep roadway under blasting disturbance. *Soil Dyn Earthq Eng*
- Reddy N, Spottiswoode S (2001) The influence of geology on a simulated rockburst. *J S Afr Inst Min Metall* 101:267–274
- Salamon M (1983) Rockburst hazard and the fight for its alleviation in South African gold mines. *Rockbursts: prediction and control*. IMM, London, pp 11–36
- Su GS, Jiang JQ, Feng XT, Mo C, Jiang Q (2016) Experimental study of ejection process in rockburst. *CJRME* 35(10):1990–1999
- Su GS, Zhai SB, Jiang JQ, Zhang GL, Yan LB (2017) Influence of radial stress gradient on strainbursts: an experimental study. *Rock Mech Rock Eng* 50(10):2659–2676
- Tan YA (1989) The mechanism research of rockburst. *Hydrogeol Eng Geol* 1(1):34–38+54
- Tan Y, Zou CJ, Wang ZB (1990) Rockburst failure characteristics and cause analysis of the diversion tunnel of Tianshengqiao II (Dam cable) Hydropower Station. In: *Water Power*, pp 22–26
- Wang JA, Park HD (2001) Comprehensive prediction of rockburst based on analysis of strain energy in rocks. *Tunn Undergr Space Technol* 16:49–57
- Wang J, Yang JX, Wu FF, Hu TF, Faisal AS (2020) Analysis of fracture mechanism for surrounding rock hole based on water-filled blasting. *Int J Coal Sci Technol* 7(4):704–713. <https://doi.org/10.1007/s40789-020-00327-y>
- Whyatt J, Blake W, Williams T, White B (2002) 60 years of rockbursting in the Coeur D'Alene District of Northern Idaho. *Lessons Learned and Remaining Issues*, USA
- Wu YJ (2019) Study on rockburst failure mechanism and stability of cavern in high geostress tunnel. Dissertation, Beijing Jiaotong University

- Xu LD, Wang LS (2001) Study on the mechanism of rockburst. *J Chongqing Univ (nat Sci Ed)* 24(2):115–117
- Yeung MR, Leong LL (1997) Effects of joint attributes on tunnel stability. *Int J Rock Mech Min Sci* 34(3–4):348
- Zhang JJ, Fu BJ (2008) Rockburst and its criteria and control. *CJRME* 27(10):2034–2042
- Zhang C, Feng XT, Zhou H, Qiu S, Wu W (2013) Rockmass damage development following two extremely intense rockbursts in deep tunnels at Jinping II hydropower station, southwestern China. *Bull Eng Geol Environ* 72:237–247. <https://doi.org/10.1016/j.ijmst.2020.03.007>
- Zhang C, Feng XT, Zhou H, Qiu S, Yang Y (2014) Rock mass damage induced by rockbursts occurring on tunnel floors: a case study of two tunnels at the Jinping II Hydropower Station. *Environ Earth Sci* 71:441–450. <https://doi.org/10.1007/s12665-013-2451-7>
- Zhang SK, Lu L, Wang ZM, Wang SD (2021) A physical model study of surrounding rock failure near a fault under the influence of footwall coal mining. *Int J Coal Sci Technol* 8(4):626–640. <https://doi.org/10.1007/s40789-020-00380-7>
- Zhou H, Meng F, Zhang C, Hu D, Yang F, Lu J (2014) Analysis of rockburst mechanisms induced by structural planes in deep tunnels. *Bull Eng Geol Environ*. <https://doi.org/10.1007/s12665-013-2451-7>
- Zhou H, Meng FZ, Zhang CQ, Lu JJ, Xu RC (2015) Effect of structural plane on rockburst in deep hard rock tunnels. *CJRME* 34(04):720–727
- Zhu FC, Song JQ (2003) Mechanical models of rock burst and its physical & numerical modeling study. *Eng Sci* 5(3):83–89
- Zhu QH, Lu WB, Sun JS, Luo Y, Chen M (2009) Prevention of rockburst by guide holes based on numerical simulations. *Min Sci Technol China* 19:346–351
- Zhu WC, Li ZH, Zhu L, Tang CA (2010) Numerical simulation on rockburst of underground opening triggered by dynamic disturbance. *Tunn Undergr Space Technol* 25:587–599. <https://doi.org/10.1007/s12665-013-2451-7>

Publisher's Note Springer Nature remains neutral with regard to jurisdictional claims in published maps and institutional affiliations.